

Solvent-induced fabrication of Cu/MnO_x nanosheets with abundant oxygen vacancies for efficient and long-lasting photothermal catalytic degradation of humid toluene vapor

Shanliang Jiang ^{a,1}, Changhao Li ^{a,1}, Yaseen Muhammad ^b, Ying Tang ^a, Ruimeng Wang ^a, Junjie Li ^a, Jing Li ^a, Zhongxing Zhao ^{a,*}, Zhenxia Zhao ^{a,*}

^a Key Laboratory of New Low-carbon Green Chemical Technology, Education Department of Guangxi Zhuang Autonomous Region, State Key Laboratory of Featured Metal Materials and Life-cycle Safety for Composite Structures, School of Chemistry and Chemical Engineering, Guangxi University, Nanning 530004, China

^b Institute of Chemical Sciences, University of Peshawar, Peshawar 25120, KP, Pakistan



ARTICLE INFO

Keywords:

Cu/Mn-based oxides nanosheets
Interfacial oxygen vacancies
 δ -MnO₂/Mn₃O₄ polycrystalline
Photothermal catalytic toluene degradation
High humidity

ABSTRACT

Construction of highly-active photothermal catalysts featuring merits of high quantum efficiency and superior heat resistance is a great challenge during volatile organic compounds (VOCs) degradation under high humidity. Herein, a facile solvent-induced dimensionality reduction strategy was proposed to engineer a nanosheeted and polycrystalline Cu/Mn-based catalyst ($M\text{-Cu/MnO}_x$) having interfacial oxygen vacancies for enhanced photothermal catalytic degradation of toluene under highly humid conditions. Unique Cu-mediated δ -MnO₂/Mn₃O₄ nanosheets with high surface area exhibited excellent light absorptivity and photogenerated carrier separation efficiency, as well as superior light-driven thermogenesis. It realized ultra-high (92.8%) toluene conversion and deep mineralization (84.4%) under RH = 80% and continuous catalytic reaction (200 h). Its toluene degradation rate exhibited 3.5–71.9 times higher than reported state-of-the-art photothermal catalysts. The newly designed M-Cu/MnO_x catalyst provides a promising, low-cost and alternative for the efficient degradation of toluene and other similar VOCs under humid conditions on large-scale operations.

1. Introduction

Volatile organic compounds (VOCs) are the main component of atmospheric pollutants and act as the precursor of photochemical smog, tropospheric ozone and secondary aerosols [1]. These VOCs are widely applied as organic solvents in chemical adhesives of building/decoration industry and hence are accidentally released into the atmosphere continuously. Their neurotoxicity and carcinogenicity result in sever threats to human life with long-term exposure even under trace concentrations [2], and hence their immediate control requires urgent attention.

A variety of strategies have been documented for the control of VOCs including adsorption [3], photocatalysis [4,5], electrocatalysis [6] and photothermal catalysis [7], etc. Among these, photothermal catalysis has received widespread attention endorsing to its excellent catalytic oxidation capacity by integrating the unique advantages of photocatalysis and thermal catalysis [8]. This coupling technology utilizes

solar energy as light and heat sources and conquers the deficiencies of poor quantum efficiency in photocatalysis and high energy consumption in thermal catalysis [9]. Besides, water vapor is ubiquitous in practical VOCs control process [10]. In this regard, designing and developing high catalytic activity and stability of photothermal catalysts for the efficient atmospheric VOCs degradation are highly urgent and challenging, especially under humid conditions.

Manganese-based oxides are one of the emerging transition-metal oxides crystalline with special characteristics including rich reserves, tunable valent-states and high abundance of oxygen species, awarding them excellent thermal catalytic activity in VOCs degradation [11]. Interfacial oxygen vacancy regulation is an effective mean to promote catalytic oxidation ability of Mn oxide species [12]. Several groups have documented reports on designing high-activity Mn-based catalysts with abundant lattice defects and oxygen vacancies. Yu et al. applied an acid-etched treatment to synthesize A-LaTi_{0.6}Mn_{0.4}O_{3+δ} with abundant surface defects and oxygen vacancies, leading to its increased toluene

* Corresponding author.

E-mail address: zhaozhenxia@gxu.edu.cn (Z. Zhao).

¹ These authors contributed equally to this work and should be considered co-first authors.

conversion of up to 96% [13]. Zhang et al. proposed a cation doping method for constructing MnCeO_x catalysts with rich-oxygen vacancies, with enhanced the adsorption of H₂O to provide HOH active sites and further promoted the photothermal catalytic activity [14]. Wu et al. reported a vacuum deoxidation strategy to prepare alpha-MnO₂/Mn₃O₄ with abundant oxygen vacancies, which strengthened the absorption of molecular oxygen and hence leading to enhanced toluene oxidation [15]. These Mn-based oxides photothermal catalysts though exhibited promoted toluene conversion, still their preparation strategies are focused to construct oxygen vacancies in bulk MnO_x phase. This is disadvantageous to light harvesting and hence require higher energy supplement to activate the oxygen vacancies for higher photothermal catalytic activity [16]. Besides, these photothermal catalysts still displayed compromised catalytic activity under high relative humidity (RH) as their band structure could not convert water into hydroxyl radicals. Therefore, engineering photothermal catalysts with abundant interfacial oxygen vacancies and superior water resistance are critical and challenging tasks to improve catalytic activity and stability in practical VOCs degradation.

Herein, a facile methanol-induced dimensionality reduction strategy is proposed to engineer interfacial oxygen vacancies and polycrystals in Mn-based oxides nanosheets (M-MnO_x and M-Cu/MnO_x) for the synergistic promotion of photo-thermal catalytic degradation of toluene. The morphology, crystal structure, porous structure and surface properties of the prepared catalysts were characterized by using scanning electron microscopy (SEM), transmission electron microscopy (TEM), N₂ adsorption and X-ray photoelectron spectroscopy (XPS). Photothermal catalytic toluene degradation performances of M-MnO_x and M-Cu/MnO_x were evaluated under different light intensities, space velocities and relative humidities. Meanwhile, plausible reaction mechanism as affected by the interfacial oxygen vacancies and polycrystalline structure in Mn-based oxide nanosheets was elaborated using oxygen temperature programmed desorption (O₂-TPD), hydrogen temperature programmed reduction (H₂-TPR), CO-consumption and in-situ DRIFT.

2. Experimental

2.1. Materials

Manganese acetate tetrahydrate (MnC₄H₆O₄·4 H₂O, 99.0%) was obtained from Sigma-Aldrich. Oxalic acid (H₂C₂O₄, 98.0%), methanol (CH₄O, 99.5%) and toluene (C₇H₈, 99.0%) were purchased from Aladdin Bio-chem technology Co. Ltd (Shanghai, China). Cupric acetate anhydrous (CuC₄H₆O₄, 98.0%) was supplied by Macklin. Pure water was produced by ultrapure water machines (Smart-S15UV, Hitech Co.). All the materials were used as received without further purification.

2.2. Synthesis of Mn-based catalysts

2.2.1. Synthesis of M-Cu/MnO_x nanosheets

Typically, MnC₄H₆O₄·4 H₂O (7.35 g, 0.03 mol) and CuC₄H₆O₄ (291 mg, 1.6 × 10⁻³ mol) were ultrasonically dissolved in 150 mL methanol, and stirred for 30 min to form a homogeneous solution. Then, equimolar oxalic acid was added to this solution and allowed to react for 50 min with vigorous stirring. The obtained precipitate was filtered and washed thrice with pure water. Subsequently, the prepared sample was dried at 80 °C overnight, and labelled as M-Cu/MnC₂O₄. The obtained M-Cu/MnC₂O₄ nanosheets were further calcinated with a heating rate of 5 °C·min⁻¹ and at 300 °C for 6 h under air atmosphere, and labelled M-Cu/MnO_x.

2.2.2. Synthesis of MnO_x with different ratios of water/methanol

To investigate the evolution of nanosheets, manganese-based oxides (MnO_x) with different morphologies were prepared by synthesizing in various water/methanol volume ratios via similar steps of M-Cu/MnO_x without the doping of copper ions. The samples prepared in pure

methanol and pure water were named as M-MnO_x and W-MnO_x, respectively. The ratios of water/methanol were set as 16%, 12% and 6%, and the corresponding samples were labelled as 16 W-MnO_x, 12 W-MnO_x and 6 W-MnO_x.

2.3. Textural characterization

Physicochemical properties of the prepared catalysts were investigated by various techniques including SEM, TEM, X-ray diffraction (XRD), Raman, Brunauer Emmett and Teller (BET), XPS, O₂-TPD, H₂-TPR, CO-consumption, UV-Vis diffuse reflectance spectroscopy (DRS), photoluminescence (PL), electrochemical impedance spectroscopy (EIS), cyclic voltammetry (CV), Mott-Schottky, electron spin resonance (ESR) spectroscopy and In-situ DRIFTS. The detailed procedures of these techniques are provided in [supplementary materials](#).

2.4. Performance test

The photothermal, thermo- and photo- catalysis of toluene oxidation were evaluated in a cylindrical stainless-steel reactor with quartz windows ([Fig. S1](#)). Reaction products were monitored by using flame ionization detector (FID) and thermal conductivity detector (TCD). The toluene conversion, CO₂ yield and toluene degradation rate were calculated using [Eqs. 1–4](#), respectively:

$$\text{Toluene degradation}(\%) = \frac{[\text{Toluene}]_{\text{in}} - [\text{Toluene}]_{\text{out}}}{[\text{Toluene}]_{\text{in}}} \times 100\% \quad (1)$$

$$\text{CO}_2 \text{ yield}(\%) (\text{mineralization ratio}) = \frac{[\text{CO}_2]_{\text{produced}}}{7 \times [\text{Toluene}]_{\text{in}}} \times 100\% \quad (2)$$

$$\text{Toluene degradation rate} = \frac{[\text{Toluene}]_{\text{in}} - [\text{Toluene}]_{\text{out}}}{\text{Mass time}} \quad (3)$$

$$\text{Mineralization ratio}(\%) = \frac{\text{CO}_2 \text{ yield}}{\text{Toluene degradation}} \times 100\% \quad (4)$$

3. Results and discussion

3.1. Morphology and textural properties

The surface morphology and elemental distribution of different solvent-induced MnO_x samples were characterized by SEM and Energy Dispersive Spectroscopy (EDS) ([Fig. 1](#)). Interestingly, their morphology was gradually evolved from sheet-stacked bulks into nanosheets, which became regular and loose with the decreasing water/methanol volume ratio during their preparation ([Fig. 1a-e](#)). Notably, the regular short-cylinder morphology was formed in 16 W-MnO_x ([Fig. 1a](#)) samples and large amounts of porous caves appeared in these secondary agglomerations with rough surface. Furthermore, thick-sheets continued to change into small amorphous particles, which aggregated into some irregular particles with 3–6 μm in 12 W-MnO_x ([Fig. 1b](#)). Upon decreasing the water ratio to 6%, 2D flake-like structure occurred in 6 W-MnO_x ([Fig. 1c](#)) and these nanosheets became thinner in M-MnO_x ([Fig. 1d](#)) that generated in pure methanol.

Mn(II) possesses strong coordination ability with oxalic acid molecules [17]. While using water as the solvent, the formed solvation shell of Mn(II)-H₂O was easily destroyed by H₂C₂O₄ and replaced H₂O from the solvation shell to coordinate with Mn(II) [18]. Fast coordination further encouraged the formation of dense and bulk MnC₂O₄ [19]. By comparison, Mn(II) was surrounded with plenty of -CH₃ groups of methanol and formed methanol solvation shell. It would produce steric hindrance to inhibit the coordination between Mn(II) and H₂C₂O₄, which slowed down the coordination kinetics in different degrees with their different lattice planes [20]. Methanol induced the oriented growth of 2D planes, resulting in nanoflake-stacked structure ([Fig. S3](#)) of

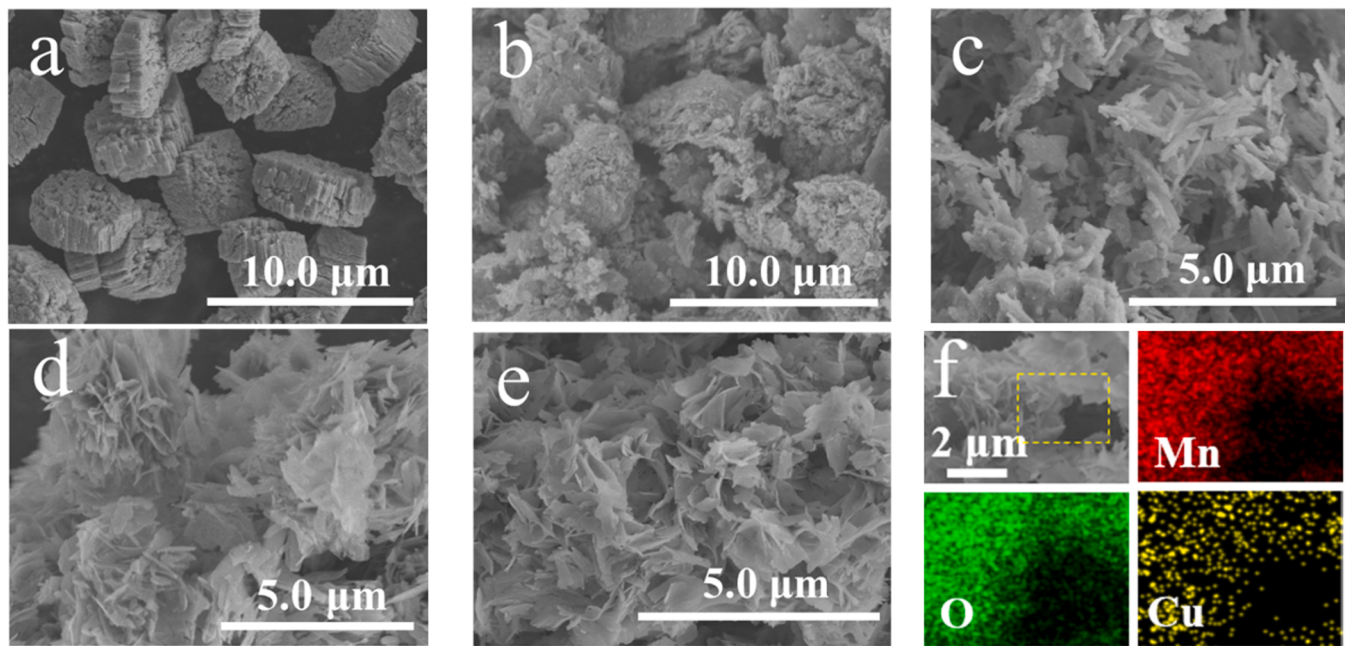


Fig. 1. SEM images of (a) 16 W-MnO_x, (b) 12 W-MnO_x, (c) 6 W-MnO_x, (d) M-MnO_x, (e) M-Cu/MnO_x; (f) SEM-EDS mapping of M-Cu/MnO_x.

M-MnC₂O₄ [21]. Subsequently, the corresponding Mn-based oxides (M-MnO_x) after annealing would keep their original nanosheeted morphology [22]. Additionally, Cu-doped M-Cu/MnO_x in Fig. 1e maintained the original flake-like structure of M-MnO_x but accumulated more loosely nanosheets. This indicated that the doping of Cu in MnC₂O₄ might facilitate to engineer Mn coordination defects in M-Cu/MnO_x [23]. The corresponding EDS elemental distribution of M-Cu/MnO_x nanosheets in Fig. 1f indicate that Mn and Cu showed a uniform dispersion in M-Cu/MnO_x nanosheets, further illustrating that the successful implantation and good dispersion of copper ions in M-Cu/MnO_x [24].

TEM crystal phase composition and nanostructures of M-Cu/MnO_x nanosheets in Fig. 2a indicate that M-Cu/MnO_x were composed of numerous conterminous nanosheets with obvious porous structure. Surprisingly, the HRTEM pattern in Fig. 2b exhibited the existence of δ-MnO₂ with (−111) crystal facets accompanied by 0.241 nm lattice spacing, as well as the presence of Mn₃O₄ with (211) crystal facets accompanied by 0.249 nm lattice spacing. There was an appealing interface generated by the crystals of δ-MnO₂ and Mn₃O₄ (marked by red line) [25,26]. Meanwhile, the presence of CuO with (202) crystal facets accompanied by 0.187 nm lattice spacing was found. The doping of copper induced lattice distortion, indicating the induction of crystal defects generation [27]. Moreover, there were numerous structures with

lattice distortion and expansion in nanosheeted M-Cu/MnO_x (marked by the green shadow) [28], which further verified the existence of abundant crystal defects.

XRD patterns of catalysts prepared with different solvent ratios and calcined MnO_x in Fig. 3a and Fig. S4 reveal the diffraction peaks of 16 W-MnC₂O₄ and 12 W-MnC₂O₄ micro-bulks were well matched with the monoclinic manganese oxalate dihydrate crystal (JCPDS PDF#25-0544) [19]. A new diffraction peak appeared at $2\theta = 11.6^\circ$ in 6 W-MnC₂O₄, which increased dramatically with methanol content, and reached the highest intensity in the pure methanol (M-MnC₂O₄ and M-Cu/MnC₂O₄ nanosheets) accompanied by the weakening peak of monoclinic manganese oxalate dihydrate crystal. The emerging peak authenticated that the methanol solvation shell would cooperate with H₂C₂O₄ molecules to realize the co-coordination toward Mn(II) [29]. This specific co-coordination structure (Fig. S5) would produce the steric hindrance, and thus induced the MnC₂O₄ to oriented growth on 2D planes [30]. It was consistent with SEM analysis (Fig. 1). After annealing, these Mn-based oxides exhibited weak diffraction peaks of coexisted δ-MnO₂ (JCPDS PDF#80-1098) and Mn₃O₄ (JCPDS PDF#80-0382) [31, 32]. Noticeably, the diffraction peaks of Mn₃O₄ continuously enhanced in intensity with increasing methanol content, and presented the highest intensity of Mn₃O₄ in M-MnO_x. This suggested that methanol solvent facilitated to regulate the generation of more Mn₃O₄, which was

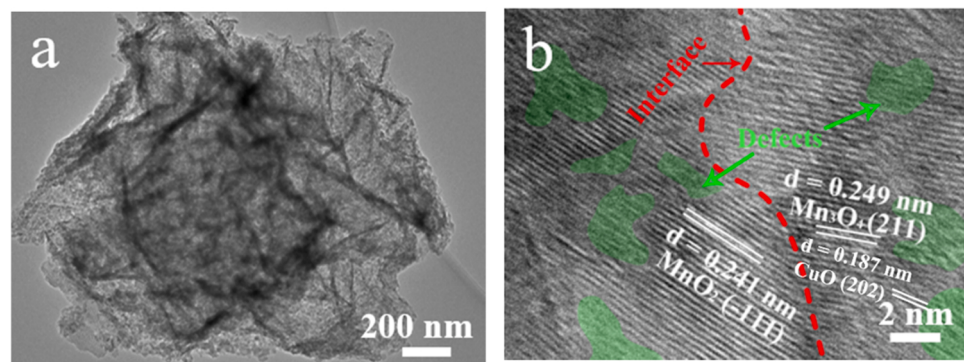


Fig. 2. (a) TEM and (b) HRTEM of nanosheeted M-Cu/MnO_x.

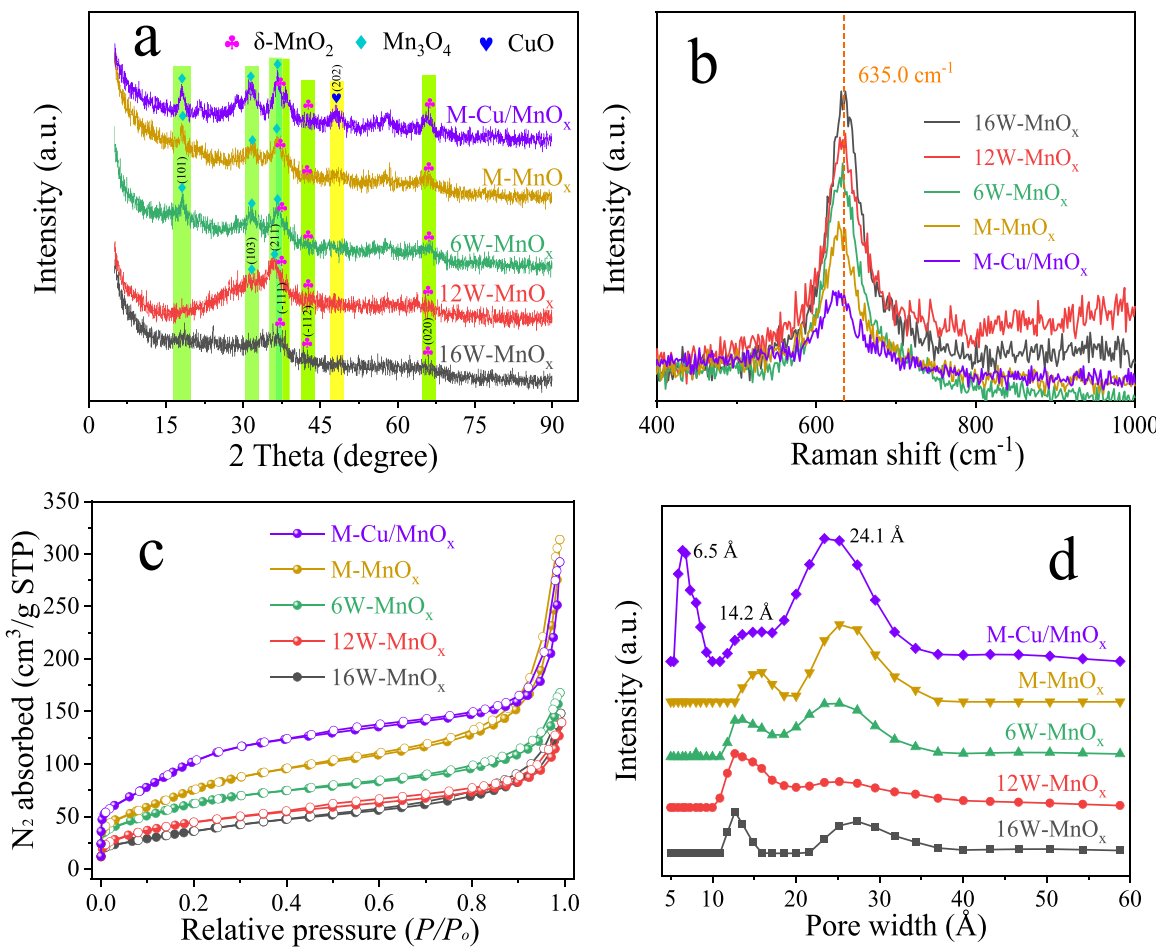


Fig. 3. (a) XRD patterns, (b) Raman spectra, (c) Nitrogen adsorption-desorption isotherms and (d) DFT pore size distributions of 16 W- MnO_x , 12 W- MnO_x , 6 W- MnO_x , M- MnO_x and M-Cu/ MnO_x .

advantageous for the occurrence of unique $\delta\text{-MnO}_2/\text{Mn}_3\text{O}_4$ polycrystalline interface [33]. Meanwhile, a weak peak attributed to CuO (JCPDS PDF#44-0706) was observed in the XRD spectrum. This result further confirmed the existence of CuO. Additionally, the half-peak-width in M-Cu/ MnO_x broadened compared to M- MnO_x , suggesting that the in-situ Cu-doping affect the MnO_6 octahedral mode, and further resulted in the intensified structure disorder and more crystal defects [11,22,34].

Raman spectroscopy in Fig. 3b show that all the samples exhibited only one broad Raman peak around 635.0 cm^{-1} , which was corresponding to the symmetric stretching vibration of Mn-O bond in the MnO_6 octahedron [35,36]. Its half-peak-width continuously broadened and weakened with the addition of methanol during its synthesis. It could be found that methanol-induced effect resulted in the occurrence of crystalline disorder and lattice defects in the MnO_6 octahedral structure, which were echoed with the SEM, TEM and XRD analyses [37]. Notably, Raman peak of M-Cu/ MnO_x nanosheets continuously decreased compared to M- MnO_x . The phenomenon further verified the formation of more defective crystals after the in-situ Cu-doping into the lattice structure of MnO_x [34]. Moreover, Raman peaks in these samples slightly shifted towards lower wavenumber with the morphology transformation, inferring the presence of weak metal-O bond induced by the crystal defects [38]. Furthermore, the insertion of copper ions in M-Cu/ MnO_x nanosheets would promote the generation of more weakened Mn-O bonds [39,40].

The N_2 adsorption-desorption isotherm and surface and pore properties of these catalysts in Fig. 3c-d and Table 1, respectively indicate that all samples presented pseudo-type IV isotherms having a steep N_2

Table 1
The physical structural parameters and surface elemental compositions.

Sample	S_{BET}^* (m^2/g)	V_t^* (cm^3/g)	V_{meso}^* (cm^3/g)	XPS $\frac{\text{Mn}^{3+}/\text{Mn}^{4+}}{\text{O}_\beta/\text{O}_\alpha}$	$\frac{\text{O}_\beta+\text{O}_\gamma}{\text{O}_\alpha}/\text{O}/\text{Mn}$	
16 W- MnO_x	138.7	0.23	0.17	0.49	0.96	2.10
12 W- MnO_x	165.8	0.26	0.18	0.62	1.05	2.06
6 W- MnO_x	234.3	0.30	0.21	0.85	1.10	1.98
M- MnO_x	297.0	0.35	0.25	0.94	1.19	1.95
M-Cu/ MnO_x	416.2	0.45	0.31	1.12	1.27	1.93

* S_{BET} : the BET surface area.

* V_t : the total pore volume of catalysts.

adsorption at low relative pressure ($P/P_0 < 0.01$) followed by a continuous increase at $P/P_0 = 0.05-0.80$ and a sharp intensified adsorption at high relative pressure region. This indicated the coexistence of hierarchical meso-micropores in these samples (Fig. 3c) [41]. 16 W- MnO_x exhibited the lowest specific surface area (SSA) ($138.7 \text{ m}^2\cdot\text{g}^{-1}$) and total pore volume ($V_t = 0.23 \text{ cm}^3\cdot\text{g}^{-1}$). With the increasing amount of methanol in MnO_x synthesis solution, the SSA and V_t of MnO_x gradually increased. By comparison, M- MnO_x synthesized in pure methanol displayed SSA and V_t values of $297.0 \text{ m}^2\cdot\text{g}^{-1}$ and $0.35 \text{ cm}^3\cdot\text{g}^{-1}$ respectively, which were 2.2 and 1.5 times higher than those of 16 W- MnO_x . This was attributed to more structural defects in MnO_x nanosheets from

its preparation via the solvent-induced strategy, and thus generated more pores in MnO_x nanosheets [13]. Notably, the SSA and pore volume were dramatically increased to 416.2 m²·g⁻¹ and 0.45 cm³·g⁻¹ after in-situ Cu doping in M-MnO_x nanosheets (M-Cu/MnO_x). Correspondingly, M-Cu/MnO_x displayed an obviously enhanced N₂ adsorption on the medium relative pressure as well as a slightly promoted in the low relative pressure. This phenomenon indicated that the in-situ Cu-doping would compete to coordinate with oxalate and distort the original Mn (II)-H₂C₂O₄ coordination mode [42]. This facilitated the M-Cu/MnO_x to form more crystal defects, and thus led to higher SSA and V_t values. Density functional theory was further carried out to calculate the pore size distribution of these samples (Fig. 3d). The result showed that all samples owned the coexisting meso-microporous structure, having pore size distribution around 14.2 and 24.1 Å. Differently, the mesoporous volume (V_{meso}) of followed an order of: 16 W-MnO_x (0.17 cm³·g⁻¹) < 12 W-MnO_x (0.18 cm³·g⁻¹) < 6 W-MnO_x (0.21 cm³·g⁻¹) < M-MnO_x (0.25 cm³·g⁻¹) < M-Cu/MnO_x (0.31 cm³·g⁻¹). Additionally, there was a new micropore (6.5 Å) occurred in M-Cu/MnO_x. Therefore, the methanol-induced sheeted morphology and the in-situ Cu-doping endowed the M-Cu/MnO_x with abundant defective meso-micropores. In summary, the increase in the specific surface area of the catalyst exposed

more catalytic active sites, improved the adsorption of toluene by the catalyst, and also promoted the generation of oxygen vacancies.

XPS measurements of 16 W-MnO_x, 12 W-MnO_x, 6 W-MnO_x, M-MnO_x and M-Cu/MnO_x in Fig. S6 show the full survey spectra of C, O, Mn and Cu elements. By calculation, their O/Mn atomic ratios followed an order of: M-Cu/MnO_x (1.93) < M-MnO_x (1.95) < 6 W-MnO_x (1.98) < 12 W-MnO_x (2.06) < 16 W-MnO_x (2.10) (Table 1). This decrease of O/Mn atomic ratio represented the increase trend of unsaturated metal-O bonds (oxygen vacancies) occurred owing to methanol regulation on their crystal defects and lattice distortion [12,43]. Notably, the introduction of Cu ions would be infused into M-MnO_x structure, and thus increased the number of oxygen vacancies on the surface of M-Cu/MnO_x nanosheets [34]. In addition, the Cu/Mn atomic ratio in M-Cu/MnO_x nanosheets was found to be about 9.1%, significantly higher than that of 5% theoretical value. This clearly proved that these rich oxygen vacancies mainly existed on the surface of M-Cu/MnO_x and accompanied by Cu ions. This further confirmed the existence of Cu-mediated polycrystalline interface of δ-MnO₂ and Mn₃O₄, which would facilitate to activate surface lattice oxygen of MnO_x [44].

The high-resolution Mn 2p XPS spectra in Fig. 4a reveal that all the samples exhibited four peaks at binding energy (BE) of 640.7, 641.9,

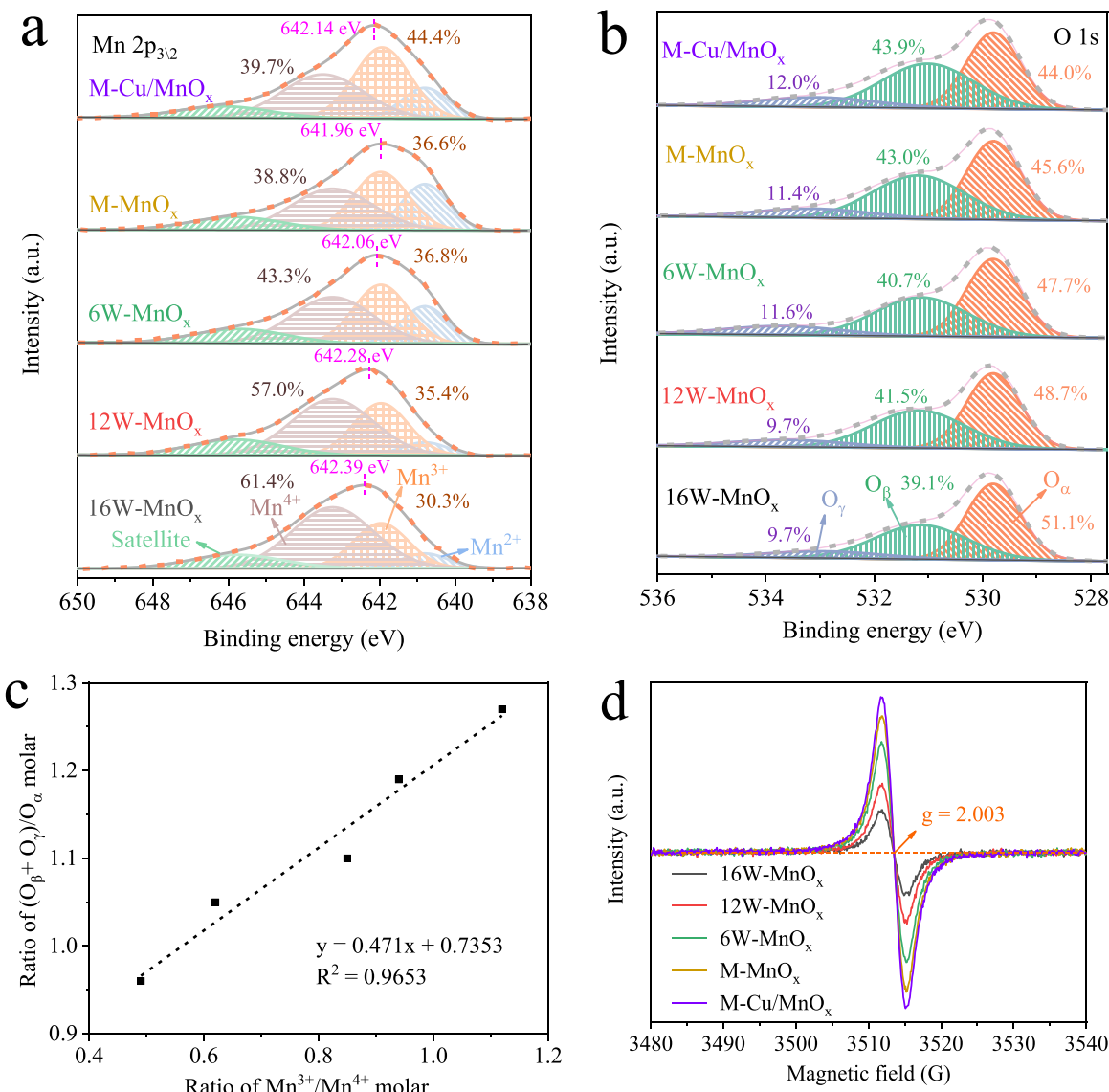


Fig. 4. (a) Mn 2p and (b) O 1s high resolution spectra of 16 W-MnO_x, 12 W-MnO_x, 6 W-MnO_x, M-MnO_x and M-Cu/MnO_x; (c) relation between ratio of (O_β + O_γ)/O_α and ratio of Mn³⁺/Mn⁴⁺ molar; (d) EPR spectra of catalysts.

643.3 and 646.0 eV, assigned to Mn²⁺, Mn³⁺, Mn⁴⁺ and satellite peaks, respectively [12,14,17]. Distinctly, there was a progressively incremental trend of the Mn^{3+/Mn⁴⁺ molar ratio in these samples with the structural transformation from bulk (16 W-MnO_x, 0.49) to flake-like (M-MnO_x, 0.94) (Fig. S7), indicating that more δ-MnO₂ crystals were converted into Mn₃O₄ crystals in the defective nanosheets [45]. In comparison, the defective M-Cu/MnO_x nanosheets presented the highest molar ratio of Mn^{3+/Mn⁴⁺ (1.12), which was 2.3 and 1.2 times higher than that of bulk 16 W-MnO_x and flake-like M-MnO_x, respectively. This thought-provoking finding further confirmed that the combination of Mn and Cu would facilitate the formation of Cu-mediated defective polycrystalline interface composed of δ-MnO₂ and Mn₃O₄, in agreement with the HRTEM result. Notably, their peaks related to Mn 2p_{3/2} performed a slightly negative shift in BE (from 642.4 to 642.0 eV) with the structural transition from bulk to nanosheets, which was attributed to}}

the increasing electron density of Mn [46]. Compared with M-MnO_x, the defective M-Cu/MnO_x nanosheets occurred an evident positive shift of Mn 2p_{3/2} peak (642.1 eV). This is because the stronger electron-withdrawing capability of Cu²⁺ than Mn ion led to the electron migration from MnO₆ toward Cu. Eventually, M-Cu/MnO_x displayed weaker metal-O bonds, leading to the increase of active oxygen species [13].

Fig. 4b shows the high-resolution O 1 s XPS spectra, which suggested three peaks at BE of 533.3, 531.2 and 529.8 eV ascribed to the adsorbed molecular water (O_γ), surface adsorbed oxygen (O_β) caused by interfacial oxygen vacancies and the lattice oxygen (O_α), respectively [47–49]. As revealed, it exhibited the boosting content of O_γ and O_β but declining content of O_α with the morphology transition from bulk to nanosheets. Thus, more unsaturated metal-O bonds were formed on the surface. The phenomenon was consistent with the Mn 2p analysis in Fig. 4a.

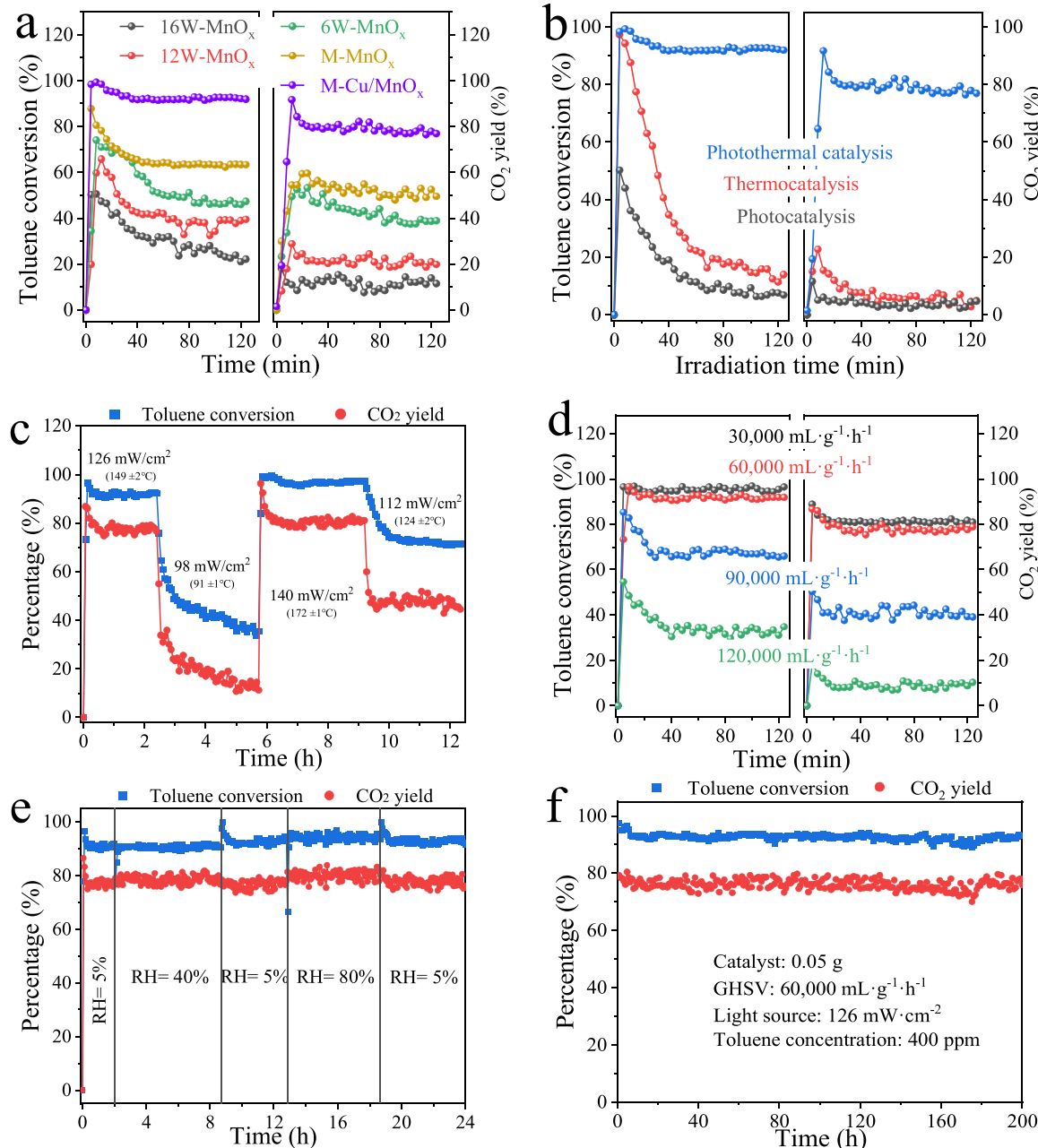


Fig. 5. Toluene conversion and CO₂ yield over the catalysts under different conditions: (a) different catalysts; and (b) different catalysis modules (photocatalytic activity at 30 °C, thermocatalytic activity at 149 °C, and photothermal catalytic activity at 149 °C, respectively), (c) diverse intensity of vis-light, (d) diverse space velocity and (e) different humidity, (f) the long-lasting catalytic capacity of M-Cu/MnO_x.

Moreover, deconvolution of O 1 s spectra in Fig. 4c exhibited that the intensity of the shoulder peak followed an order of: 16 W-MnO_x (0.96) < 12 W-MnO_x (1.05) < 6 W-MnO_x (1.10) < M-MnO_x (1.19) < M-Cu/MnO_x (1.27). As shown, these samples possessed a good linear correlation ($R^2 = 0.97$) between the ratio of $(O_\gamma + O_\beta)/O_\alpha$ and the molar ratio of Mn³⁺/Mn⁴⁺. This provided the clear evidence that the occurrence of Mn³⁺ in MnO₂ would be more advantageous for the formation of abundant oxygen vacancies [15]. Additionally, the Cu-mediated MnO₂-Mn₃O₄ interface would produce a positive affect toward the generation of more defective oxygen vacancies, which would endow the defective M-Cu/MnO_x nanosheets with excellent redox ability.

To gain further insight into the content of interfacial oxygen vacancies in these solvent-induced samples, EPR measurements were employed and the result is shown in Fig. 4d. Apparently, all samples displayed symmetrical Lorentzian curves at the Lande-factor $g = 2.003$, typically attributed to the unpaired electrons in the oxygen vacancies and further reflected the concentration of oxygen vacancies through the signal intensity. Noteworthily, the EPR signal intensity of these samples boosted gradually with the increasing methanol content in the synthesis system. As expected, nanosheeted M-Cu/MnO_x revealed the highest signal intensity, demonstrating that the doping of copper promoted the lattice distortions in MnO_x and further enhanced the content of oxygen vacancies. These intriguing aspects verified that the synergistic effect of methanol-induced dimensionality reduction strategy and in-situ Cu-doping played a stimulated role to improve the content of oxygen vacancies, which could possibly boost photothermal catalysis.

3.2. Light-driven photothermal catalytic performance

The photothermal catalytic performance of different solvent-induced samples in terms of light-driven (126 mW·cm⁻²) toluene degradation is shown in Fig. 5a, where all samples displayed the sharp increase of toluene conversion and CO₂ yield within the first ten minutes, and followed by varying degrees of decline onward. Interestingly, the 16 W-MnO_x bulk displayed the smooth toluene conversion of 22.3% and CO₂ yield of 19.2% within 120 min. With the structural transformation from bulk to sheeted M-MnO_x, gradually elevated the toluene conversion to 63.4% and CO₂ yield to 50.4%. Noticeably, defective M-Cu/MnO_x nanosheets exhibited further boosted toluene conversion up to 92.8% and CO₂ yield up to 78.3%, which was 4.2 times higher than that of 16 W-MnO_x.

For elucidating the photothermal synergy in the efficient toluene degradation, pure thermo-catalytic and photocatalytic tests were carried out and the findings are shown in Fig. 5b and Fig. S8. The quick deactivation of the catalysts for toluene degradation was observed under photocatalytic and thermocatalytic conditions. Meanwhile, the actual yield of CO₂ was much lower than the theoretical yield of CO₂ calculated from the degradation ratio of toluene. It was inferred that this catalyst cannot achieve complete mineralization of toluene molecules only under photocatalytic or thermocatalytic conditions. This was speculated that a certain intermediates were generated and then accumulated on the active sites of the catalyst [50], resulting in an obvious decrease in the catalytic activity of the catalyst. On the contrary, toluene conversion in M-Cu/MnO_x nanosheets kept very high level with reaction time under photothermal catalytic condition, which was nearly 6.6 and 12.7 times higher than that of the pure thermal-driven and pure photocatalytic processes (Fig. 5b). This phenomenon was also observed in these series MnO_x catalysts (Fig. 5a and Fig. S8). Clearly, it verified the synergistic effect of photo- and thermo- catalytic process in toluene degradation. Moreover, the toluene conversions under both thermo- and photo-catalytic process increased with the dimensionality reduction of MnO_x catalysts (Fig. S8). This indicated that the change in catalyst morphology from bulk to flake increased the concentration of interfacial oxygen vacancies, which in turn increased the catalytic activity [51]. Furthermore, the photocatalytic and thermocatalytic properties of Cu-doped M-Cu/MnO_x were improved to a certain extent compared with

M-MnO_x (Fig. S8).

The effect of light irradiation intensity on photothermal catalytic activity of defective M-Cu/MnO_x nanosheets was explored and the results are shown in Fig. 5c. It suggested that M-Cu/MnO_x nanosheets realized toluene conversion of up to ~ 93% accompanied by CO₂ yield of ~ 79% under light irradiation intensity of 126 mW·cm⁻². Synchronously, the temperature produced by the light-driven thermogenesis was 149 °C in the photothermal catalytic system. The photothermal catalytic performance of M-Cu/MnO_x gradually decreased with the decline of light irradiation energy. When the light irradiation intensity was increased, the photothermal catalytic activity of M-Cu/MnO_x nanosheets increased again. Under the light irradiation intensity of 140 mW·cm⁻², the light-driven temperature of M-Cu/MnO_x reached to 172 °C, and its photothermal catalytic ability reached the maximum value (97% toluene conversion and 81% CO₂ yield). This was only a slight increase compared to that under 126 mW·cm⁻² light irradiation, demonstrating the oversupplied energy under 140 mW·cm⁻² [24]. Thus, the light irradiation intensity of 126 mW·cm⁻² was chosen for onward experiments.

The results of the effect of space velocity on the toluene oxidation capacity per unit time and unit quality of M-Cu/MnO_x catalysts in Fig. 5d indicate that toluene conversion efficiency declined with increasing space velocity from 30,000 to 120,000 mL·h⁻¹·g⁻¹ by using 400 ppm toluene and 126 mW·cm⁻² light irradiation. Among the various catalysts, M-Cu/MnO_x nanosheets displayed the highest toluene conversion (96%) and CO₂ yield (81%) under the 30,000 mL·h⁻¹·g⁻¹ space velocity. The photothermal catalytic performance remained unchanged even increasing space velocity to 60,000 mL·h⁻¹·g⁻¹ (93% toluene conversion and 79% CO₂ yield). As reflected by Fig. S9, M-Cu/MnO_x showed 1.95 times higher toluene degradation rate (0.792 μmol·g⁻¹·min⁻¹) under 60,000 mL·h⁻¹·g⁻¹ than that under 30,000 mL·h⁻¹·g⁻¹ (0.407 μmol·g⁻¹·min⁻¹), while the CO₂ yield was indistinguishable. This provided the clear evidence that defective M-Cu/MnO_x nanosheets had better toluene oxidation capacity per unit time and unit quality of catalyst under 60,000 mL·h⁻¹·g⁻¹ space velocity than under 30,000 mL·h⁻¹·g⁻¹ space velocity. However, the toluene conversion dramatically decreased to 66% and 33% as well as the CO₂ yield decreased to only 40% and 10% by increasing space velocity to 90,000 and 120,000 mL·h⁻¹·g⁻¹, respectively. This indicated that the exorbitant space velocity results in decreasing the resistant time of toluene with M-Cu/MnO_x. The inadequate exposure time led to the dramatic decrease in photothermal catalytic performance for toluene [52]. Eventually, the space velocity of 60,000 mL·h⁻¹·g⁻¹ was opted as the optimum value for the efficient toluene photothermal catalytic degradation.

RH was engaged to investigate the steam resistance properties of the defective M-Cu/MnO_x nanosheets, and the results are shown in Fig. 5e. The defective M-Cu/MnO_x nanosheets showed excellent toluene conversion of 93% and CO₂ yield of 79% under RH of 5%. Interestingly, these values of toluene conversion and CO₂ yield maintained very stable with increasing RH from 40% to 80%. This demonstrated enhanced water resistance of the defective M-Cu/MnO_x nanosheets during toluene photothermal catalysis. Additionally, a continuous reaction experiment was also employed to identify the catalytic durability of the M-Cu/MnO_x nanosheets under optimum condition (Fig. 5f). As shown, the toluene conversion and CO₂ yield were constantly maintained around 91% and 77% respectively after 200 h of continuous catalytic reaction. This result was much longer than many reported catalysts and indicated the excellent photothermal catalytic stability of M-Cu/MnO_x nanosheets [15].

In order to investigate the structural stability of M-Cu/MnO_x nanosheets, PXRD and XPS analyses were performed after 200 h of continuous photothermal catalysis degradation of toluene and the results are shown in Fig. S10. It is seen from Fig. S10a that M-Cu/MnO_x nanosheets maintained the original crystal structure after the consecutive photothermal catalysis, which was attributed to the avoidance of

agglomeration by the catalytic active component on M-Cu/MnO_x [15]. Additionally, based on the Mn 2p, O 1s and Cu 2p XPS analysis (Fig. S10b-d), it is noted that the used M-Cu/MnO_x nanosheets retained similar peak profile and valence content distribution of Mn³⁺/Mn⁴⁺, (O_β+O_γ)/O_α as well as Cu⁺/Cu²⁺. This phenomenon further confirms the excellent stability of the defective M-Cu/MnO_x nanosheets during toluene degradation, and hence paves its route for large-scale applications.

The photothermal catalytic performance of defective M-Cu/MnO_x nanosheets was compared with reported catalysts under identical experimental conditions [47,53,54]. The toluene degradation rate (Eq. 3) was compared with reported catalysts and shown in the inset of Fig. 6. The toluene degradation rate ($0.792 \mu\text{mol}\cdot\text{g}^{-1}\cdot\text{min}^{-1}$) of M-Cu/MnO_x nanosheets rich in oxygen vacancies was 2.7–5.9 times higher than the reported photothermal catalysts. The photothermal catalytic ability is defined as the ratio of the toluene degradation rate per unit light irradiation intensity, which was further employed to evaluate the available energy utilization of these catalysts toward toluene degradation (Fig. 6). Distinctly, the defective M-Cu/MnO_x nanosheets exhibited $13.66 \mu\text{mol}\cdot\text{g}^{-1}\cdot\text{min}^{-1}\cdot\text{mW}^{-1}\cdot\text{cm}^2$, about 3.5–71.9 times higher than those reported state-of-the-art costly catalysts. This astonishing result confirmed that defective M-Cu/MnO_x nanosheets displayed more outstanding utilization and conversion of the energy supplied, which would facilitate the enhancement of photothermal catalytic ability for VOCs abatement even in highly humid environments.

3.3. Synergistic effects of photo- and thermo- activation on MnO_x photothermal catalysts

3.3.1. Optical property

Physicochemical properties of these catalysts with different solvent ratios were characterized via UV-Vis DRS, PL spectroscopy, EIS and CV. The UV-Vis DRS findings in Fig. 7a indicate that all the samples exhibited light absorption in both UV and visible regions due to the inherent nature of dark-colored Mn-based oxides [53]. Noteworthily, the absorption spectrum was gradually reinforced with the morphology transition from bulk-like (16 W-MnO_x) to flake-like (M-MnO_x), especially in the visible region. This phenomenon indicated that porous nanosheets M-MnO_x with crystal interface and more surface oxygen vacancies could broaden optical absorption and spectral response range [55,56]. Additionally, M-Cu/MnO_x nanosheets presented the highest light-adsorption performance. This may be due to the enhanced UV-vis absorption capacity of dispersed CuO_x [57]. Therefore, the light-driven thermogenesis of these catalysts ranked in an order of: 16 W-MnO_x (137°C) < 12 W-MnO_x (139°C) < 6 W-MnO_x (142°C) < M-MnO_x (143°C) < M-Cu/MnO_x (149°C) (Fig. S11).

To analyzed the charge recombination/separation, and electron transfer of the photothermal catalysts with different solvent ratios, PL spectroscopy and EIS curves were conducted and showed in Fig. 7b-c. As

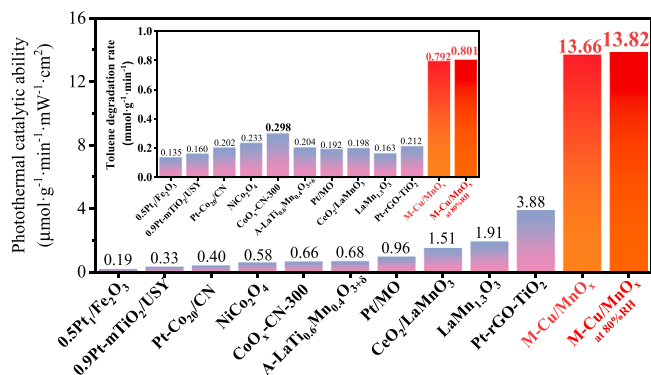


Fig. 6. The photothermal catalytic ability of the catalyst reported in the literature and in this work.

revealed, the PL intensity of these samples declined with the solvent-regulated structural transition from bulk 16 W-MnO_x to flake-like M-MnO_x. With the addition of methanol in MnO_x precursor synthesis, the obtained MnO_x exhibited high trapping ability for photogenic electron, and thus high ability for electron-hole pair separation due to their increase interfacial oxygen vacancies [58]. As expected, M-Cu/MnO_x nanosheets displayed the lowest PL intensity. Similarly, Nyquist plots displayed semicircles of these MnO_x, and showed charge transfer resistance values in an order of: M-Cu/MnO_x (91.8Ω) < M-MnO_x (116.5Ω) < 6 W-MnO_x (142.6Ω) < 12 W-MnO_x (172.6Ω) < 16 W-MnO_x (308.7Ω). With ditto, the charge transfer resistance values of these samples diminished with the decreased water/methanol ratio, indicating the improved conductivity with the increase of methanol content in MnO_x precursor synthesis. Moreover, the in-situ Cu dopant in MnO_x was advantageous for the fast electron transportation and further promoted the photogenerated carrier spatial separation [59], which was mainly attributed to the generation of more interfacial oxygen vacancies along with the interface of MnO₂ and Mn₃O₄ mediated by Cu. Attributed to this rewarding aspect, M-Cu/MnO_x nanosheets with abundant oxygen vacancies and unique polycrystalline interface intensified the electron transfer ability [60] and possessed satisfactory photogenerated carrier separation efficiency. These results led to the enhancement of photocatalytic activity.

The redox abilities of different catalyst-modified electrodes were evaluated by CV measurements and the results are shown in Fig. 7d. As seen, all samples displayed symmetric double peaks. Notably, with the solvent-regulated structural transition from bulk 16 W-MnO_x to flake-like M-MnO_x, the potential separation ($\Delta E_p = E_{pa} - E_{pc}$) values gradually decreased while the peak current response (I_p) values increased. This intriguing variation indicated that the defective nanosheets induced by solvent effect had more abundant Mn³⁺|Mn⁴⁺ polycrystalline interfaces, which were conducive for the elevation of redox ability [28]. Moreover, M-Cu/MnO_x nanosheets possessed the smallest ΔE_p and highest ΔI_p values. It was benefited from the enhanced electron transfer and the redox activity from Cu-mediated Mn³⁺|Mn⁴⁺ polycrystalline interfaces [61]. To further explore the electrochemical stability of M-Cu/MnO_x, CV measurement was conducted and the results are shown in the inset of Fig. 7d. Surprisingly, M-Cu/MnO_x nanosheets displayed excellent redox stability after 50 times consecutive CV tests. It further verified that the unique Cu-mediated Mn³⁺|Mn⁴⁺ polycrystalline interfaces endowed M-Cu/MnO_x with superior internal electron transmission ability and Mn valent reversibility. This was conducive for boosting the redox stability, and thus promoted photothermal catalytic degradation of toluene.

3.3.2. Evaluation of thermal-assisted photo-catalytic activity

To further confirm the photocatalytic activity of M-Cu/MnO_x nanosheets, ESR spectroscopy measurements (Fig. 8a) was used to investigate the generation and transformation of reactive oxygen species (ROS, including ·O₂ and ·OH). There existed almost no signal peaks of DMPO-·O₂ and DMPO-·OH in M-Cu/MnO_x under dark and without-heating conditions. Intriguingly, these two characteristic sextet signals appeared after light irradiation, demonstrating the generation of plenty of ·O₂ and ·OH radicals in the system [4,62]. Meanwhile, photogenerated hole trapping experiments were performed, and the 1:1:1 triple peak signal of TEMPO feature was significantly weakened under light conditions (Fig. S12). This indicated that the material generates large amount of e⁻/h⁺ under light conditions, which promotes the generation of ·O₂ and ·OH. To investigate the photocatalytic mechanism of M-Cu/MnO_x, UV-Vis DRS and Mott-Schottky measurement of δ-MnO₂ and Mn₃O₄ were utilized to represent the heterojunction structure of Cu/MnO_x (Fig. S13). As illustrated, M-Cu/MnO_x nanosheets were mainly composed of δ-MnO₂ and Mn₃O₄ (TEM and XRD results). From UV-Vis DRS spectra, pure δ-MnO₂ and Mn₃O₄ exhibited transition bandgap energies of 1.62 and 1.93 eV respectively [15,63] (Fig. S13a-b). Furthermore, the flat-band potentials (E_{fb}) of δ-MnO₂ and Mn₃O₄ were

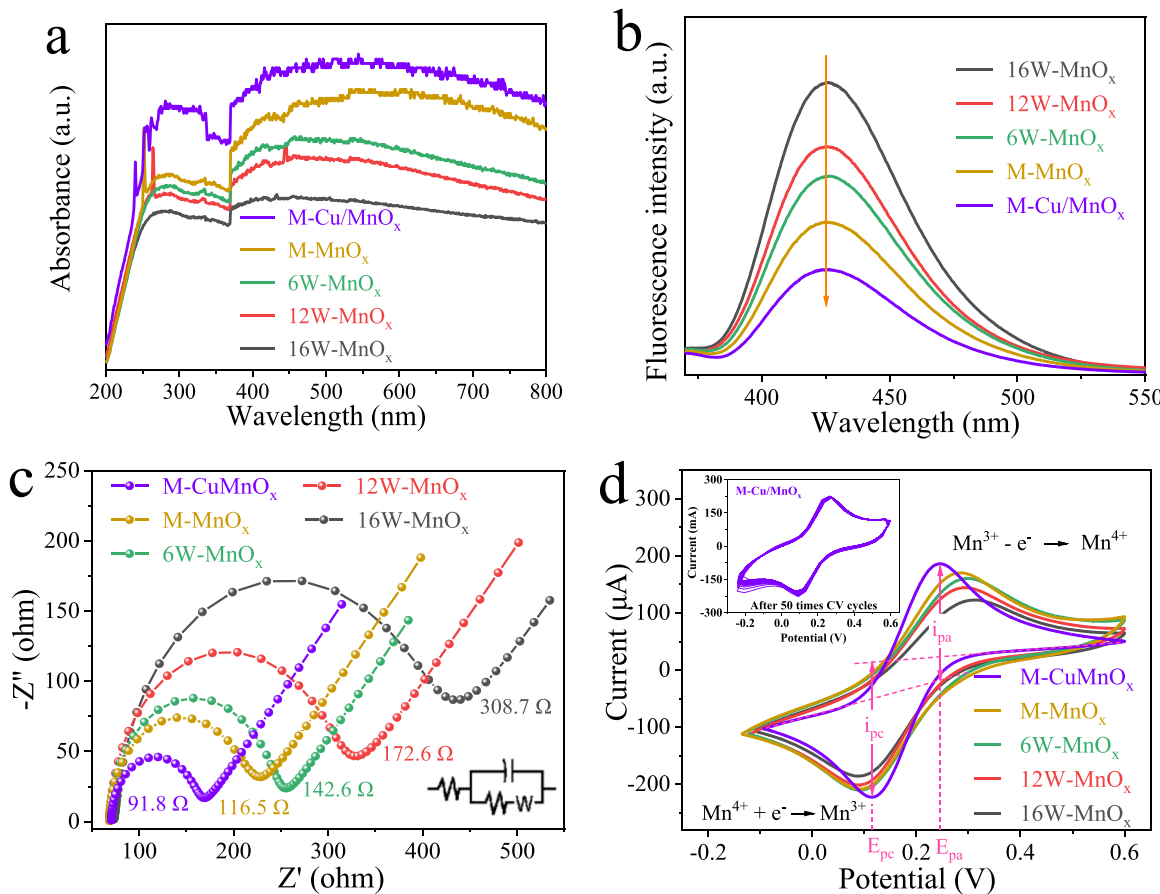


Fig. 7. (a) UV-Vis DRS spectra, (b) PL emission spectra, (c) EIS Nyquist diagrams and (d) CV curves over the catalysts.

deduced through the Mott-Schottky method by projecting the different frequencies intersect on the x-axis of the corresponding edges (Fig. S13c-d), and were calculated to be 0.37 V and –0.56 V respectively. Both the samples presented positive slopes, suggesting that the nature of n-type semiconductor of δ -MnO₂ and Mn₃O₄ was estimated to be 0.56 and –0.37 eV with respect to the normal hydrogen electrode [4]. Thus, their calculated corresponding valence band potentials (E_{VB}) were 2.18 and 1.56 eV, separately. Combined with ESR results of M-Cu/MnO_x, the band structure of M-Cu/MnO_x could only match Z-scheme heterojunction model (Fig. 8b) instead of type-II heterojunction (Fig. S14). Obviously, the E_{VB} of δ -MnO₂ was accessibly higher than the potential for the oxidation of H₂O/OH[–] into ·OH (1.99 eV) [64], which could boost h⁺ of δ -MnO₂ to produce ·OH via oxidizing H₂O/OH[–]. Subsequently, the excited electrons in CB of δ -MnO₂ could migrate across the “upward” bent conduction band (CB) to the valence band (VB) of Mn₃O₄ and recombine with h⁺. This could facilitate spatial charge separation [65,66]. Concurrently, the photogenerated electrons of Mn₃O₄ were transferred to CB level, and then transferred to CuO_x, which would boost the conversion of absorbed O₂ into O^{2–} (–0.33 eV) [15]. CuO_x enhanced interfacial electron conduction and improved the separation efficiency of photogenerated electrons and holes. Copper doping also led to the generation of lattice defects. This promoted the generation of large number of interfacial oxygen vacancies. Meanwhile, interfacial oxygen vacancies, as a kind of defect energy level below CB level could efficiently trap these photogenerated electrons [67]. Moreover, the synergistic effect of Z-scheme heterojunction and interfacial oxygen vacancies generate more ROS by accelerating the separation of e[–]/h⁺ pairs. This endowed the catalyst with high redox ability for toluene degradation.

To further evaluate the boosting effect of thermal activation in photothermal catalysis, the Mott-Schottky plots of M-Cu/MnO_x

nanosheets under different temperatures were carried out (Fig. 8c). As presented in Fig. S15, the flat-band potential values deduced from the Mott-Schottky method of M-Cu/MnO_x were significantly decreased (from 0.612 to –0.048 V) with the stepwise rise in temperature from 25° to 70°C. This variation indicated that thermal activation accelerated the photogenerated electrons transfer from VB level and interfacial oxygen vacancies transitioning to the CB level. This efficiently inhibited the photogenerated e[–]/h⁺ recombination on M-Cu/MnO_x nanosheets, and thus achieved the rapid generation of ROS. Thus, photogenerated-electrons excited by thermal activation played a curtail role in efficient photothermal synergistic catalytic degradation of toluene under the presence of H₂O vapors.

3.3.3. Photo-assisted thermal-catalytic activity

The synergistic effect of photothermal catalysis was investigated by using H₂-TPR, O₂-TPD and CO-consumption profiles of the catalysts under illumination and dark conditions as shown in Fig. 9. H₂-TPR curves were further performed to evaluate the reduction capability of the catalysts synthesized with different CH₃OH/H₂O solvent ratios. As revealed from Fig. 9a, MnO_x included two main reduction peaks in H₂-TPR curves. The first peak at 240–294 °C (labelled as C_{TI-H2}) was ascertained to the reduction amounts of surface adsorbed oxygen species and the conversion of Mn⁴⁺ into Mn³⁺ [61]. The second peak at 405–440 °C (labelled as C_{III-H2}) was related to the complete reduction of Mn³⁺ (including the Mn³⁺ reduced by R_I and the original Mn³⁺) into Mn²⁺ [68]. Interestingly, the H₂ consumption amount of C_{TI-H2} in these MnO_x gradually increased with the reduced dimension of structure from bulk to sheet, and followed a sequence of 16 W-MnO_x (2089.5 μmol·g^{–1}) < 12 W-MnO_x (3007.5 μmol·g^{–1}) < 6 W-MnO_x (3309.7 μmol·g^{–1}) < M-MnO_x (3595.4 μmol·g^{–1}) < M-Cu/MnO_x (3930.8 μmol·g^{–1}) (Table S2). According to this, M-Cu/MnO_x nanosheets displayed 1.9 and

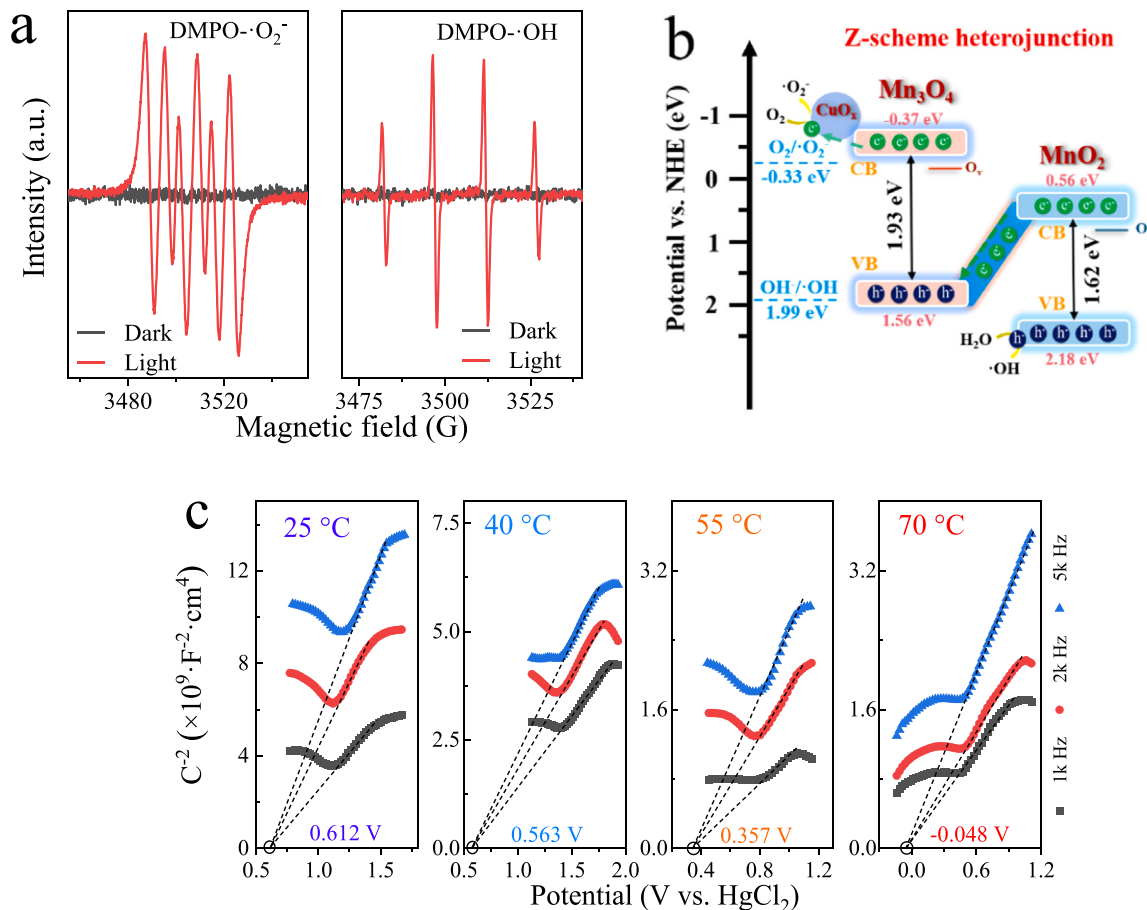


Fig. 8. (a) ESR spectra, (b) Z-scheme heterojunction and (c) In-situ Mott-Schottky curves of M-Cu/MnO_x.

3.3 times higher $C_{\text{Ti-H}_2}$ value than that of M-MnO_x and 16 W-MnO_x, respectively. Meanwhile, the overall curves in MnO_x presented apparent peak shift toward lower temperature with the structure dimensionality reduction. It could be attributed to the increment of surface adsorbed oxygen species in these MnO_x with morphology evolution, and thus reduced their catalytic activation temperature [61]. This indicated that the synergistic effect of methanol-induced dimensional reduction and Cu doping endowed M-Cu/MnO_x nanosheets with excellent low-temperature reduction performance.

For exploring the reduction capacity of Mn-based oxides under photo-thermal condition, vis-light was introduced into the H₂-TPR to further assess the photothermal synergistic effect on the reduction behaviors. As shown in the solid lines of Fig. 9a, all the catalysts displayed appreciable peak shift toward lower temperatures under photo irradiation. Noticeably, the low-temperature peak of M-MnO_x presented greater shift than high-temperature peak in the H₂-TPR curves. This phenomenon suggested that the surface adsorbed oxygen species and Mn⁴⁺ owned better reduction ability and lower reduction temperature under photothermal conditions with increasing methanol content. Moreover, the initial H₂ consumption rate [16] at low temperature was applied to study the differences of reduction in those catalysts, and the results are shown in Fig. 9b and Table 2. With the solvent-regulated structural transition, the low-temperature reduction ability of MnO_x catalysts was easier not only in pure thermal but also under photo irradiation condition. Moreover, the value of initial H₂ consumption rate under photo irradiation ($R_{\text{P-H}_2}$) was higher than that of pure thermal condition ($R_{\text{T-H}_2}$). Among them, the difference between light irradiation and pure thermal condition ($\Delta R_{\text{P-T}}$) on M-Cu/MnO_x nanosheets was 19.3, which was much greater than that of M-MnO_x (11.8) and 16 W-MnO_x (4.7) (Table 2). This adequately demonstrated that the

synergistic enhancement of light trapping capacity and photothermal conversion effect could effectively improve the low temperature catalytic activity. As expected, M-Cu/MnO_x with the strongest reduction capability exhibited the best photothermal catalytic activity for toluene oxidation.

O₂-TPD spectra of W-MnO_x, M-MnO_x, and Cu-doped M-Cu/MnO_x were conducted to investigate their activation and mobility of active oxygen species under pure thermal-driven and photo-thermal treatments. Notably, all of their O₂-TPD curves displayed two apparent peaks at approximately 465–535 °C and 703–773 °C under pure thermal-driven condition. These peaks were assigned to the surface lattice oxygen species (labelled as O_{surf}) and bulk lattice oxygen (labelled as O_{latt}) respectively (Fig. S16) [12,69]. Distinctly, the intensity of O_{surf} was gradually increased with their morphology transformation from bulk to flake-like, which was contrary to that of bulk O_{latt}. Likewise, their peaks of O_{surf} shifted toward lower temperature with the dimensionality reduction. These phenomena became more obvious in M-Cu/MnO_x nanosheets, implying that structural dimensionality reduction could provide more surface lattice oxygen species in those MnO_x to participate in redox reaction [70]. Additionally, a broad peak ahead of O_{surf} appeared in 6 W-MnO_x, M-MnO_x, and M-Cu/MnO_x, belonging to the adsorbed oxygen species from their oxygen vacancies (labelled as O_v). This peak also showed a clear shift towards lower temperatures in M-Cu/MnO_x nanosheets, which exhibited similar trend to O_{surf} peak. The increasing peak intensity and forward shift signified the increasing amount and promoting reaction activity of O_v and O_{surf}. In general, these changes in M-Cu/MnO_x nanosheets are conducive to enhance toluene catalytic performance under thermal-driven catalysis [43].

Similarly, vis-light irradiation was introduced into the O₂ adsorption prior to O₂-TPD process to simulate photo-thermal driven catalytic

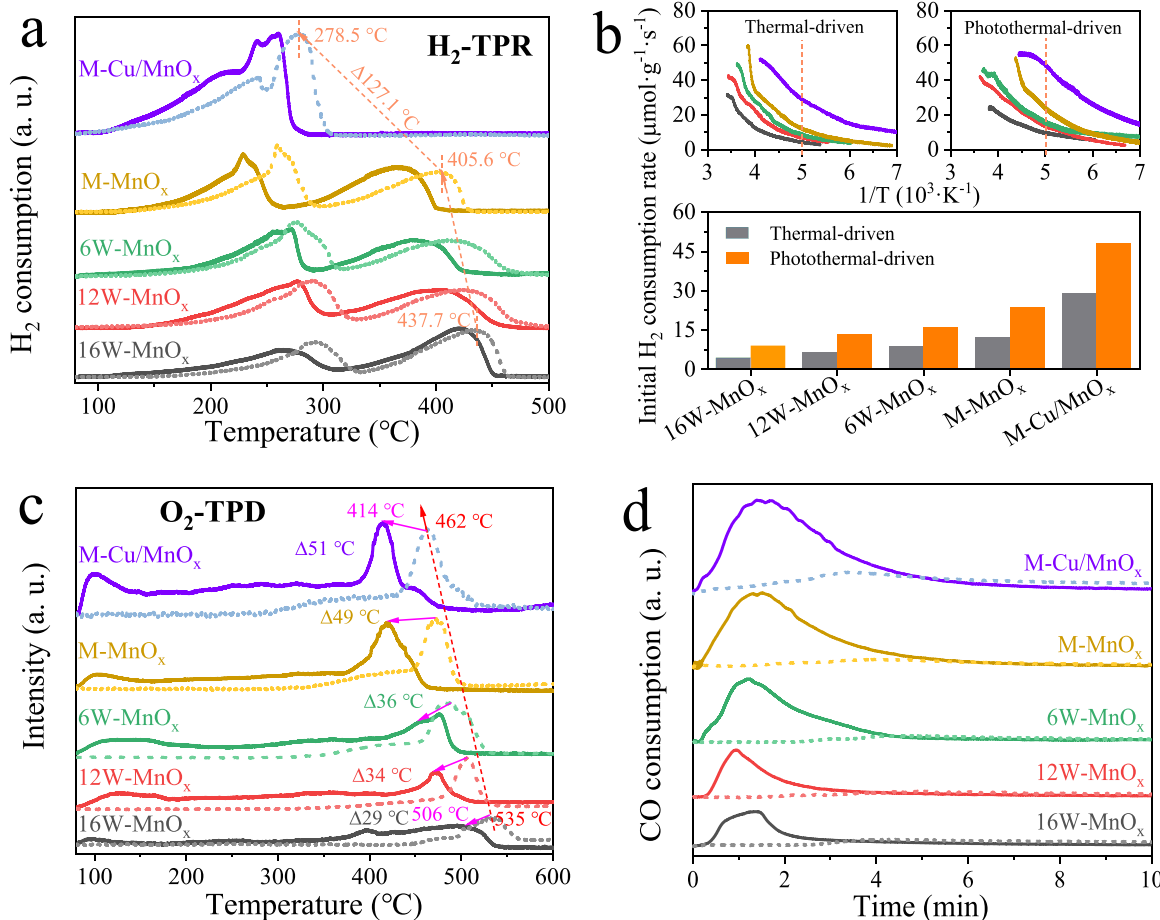


Fig. 9. (a) H₂-TPR curves and (b) their initial H₂ consumption rate; (c) O₂-TPD; (d) CO-consumption profiles of catalysts under photothermal-driven (solid lines) and pure thermal-driven (dotted lines) conditions.

Table 2
The parameters of H₂-TPR and CO-consumption over the catalysts.

Sample	H ₂ consumption rate (μmol·g ⁻¹ ·s ⁻¹)			CO consumption (μmol/g)		
	R _{T-H2}	R _{P-H2}	ΔR _{P-T}	C _{T-CO}	C _{P-CO}	C _{P-CO} /C _{T-CO}
16 W-MnO _x	4.37	9.06	4.69	9.3	37.9	4.1
12 W-MnO _x	6.60	13.43	6.83	9.5	45.8	4.8
6 W-MnO _x	8.96	16.10	7.14	9.6	86.0	8.9
M-MnO _x	12.14	23.93	11.79	9.9	108.3	10.9
M-Cu/MnO _x	28.94	48.23	19.29	12.3	158.8	12.9

RT-H2, RP-H2 and ΔRP-T: H₂ consumption rates of pure thermal-driven, photothermal treatments, and their difference between these two processes; C_{T-CO} and C_{P-CO}: CO consumptions of pure thermal-driven and photo-thermal treatments.

process (Fig. 9c). Interestingly, a new and clear peak of O₂ desorption appeared at approximately 80–200 °C compared to their pure thermal-driven system. Considering the desorption temperature range, this peak should refer to the O₂ desorption on MnO_x surface through a relative weak chemisorption (labelled as O_c) under light irradiation [43]. The peak intensity of O_c significantly increased with dimensionality reduction of MnO_x, which indicated that photo irradiation would enhance adsorption affinity of MnO_x surface towards O₂ and hence promote O₂ capture [53]. Besides, the desorption peak temperature of O_v and O_{surf} were significantly offset toward lower temperatures with higher peak intensity, accompanied by the dimensionality reduction of MnO_x. As shown, the O_{surf} desorption temperature difference of these samples under photo-thermal and pure thermal-driven condition

followed an order of: 16 W-MnO_x (29 °C) < 12 W-MnO_x (34 °C) < 6 W-MnO_x (36 °C) < M-MnO_x (49 °C) < M-Cu/MnO_x (51 °C). These results manifested that solvent-induced defective flake-like structure possessed better light-harvesting capacity and more superior light-to-heat ability. In addition, copper oxide is easily reduced due to the weak bonding interaction between Cu and atomic oxygen. The valence cycle of copper also promotes the cycle between Mn³⁺/Mn⁴⁺. The low bond dissociation energy of Cu-O bonds is expected to accelerate more metal-O bond breaking to desorb more ROS [71,72]. In conclusion, light-driven photo-thermal effect verified the synergistic ascension of O₂ capture and its activation, and promoted photothermal catalytic activity toward toluene oxidation on M-Cu/MnO_x nanosheets.

The activity of surface oxygen species during photothermal and thermal conditions was evaluated by CO-consumption experiments (Fig. 9d). MnO_x exhibited faint peaks of CO consumption in pure thermal-driven condition (C_{T-CO}) with the morphology transformation from bulk to nanosheet, whereas it showed a slightly increased peak intensity in M-Cu/MnO_x nanosheets (Table 2). This proved that the surface oxygen species were hard to be activated under low-temperature thermo-catalysis for CO oxidation. Comparatively, the CO consumptions of these catalysts were significantly incremental under photothermal-driven condition (C_{P-CO}). Interestingly, the value of CO consumption in M-Cu/MnO_x (158.8 μmol·g⁻¹) was 4.2 times and 1.5 times higher than that of 16 W-MnO_x (37.9 μmol·g⁻¹) and M-MnO_x (108.3 μmol·g⁻¹), respectively. Among with pure thermal-driven and photo irradiation, the C_{P-CO}/C_{T-CO} ratio value of 16 W-MnO_x was calculated to be 4.1, while this value was further increased to be 10.9 in M-MnO_x and 12.9 in M-Cu/MnO_x. This once again verified the synergistic effect of photo irradiation and thermal-driven promoted the activation of surface

oxygen species at low temperature to generate more active oxidants, and thus the photothermal catalytic activity of toluene was much better than that of pure thermo-catalysis.

3.4. Proposed reaction pathway

In-situ DRIFTS measurements were applied to further understand the reaction mechanism of toluene oxidation on M-Cu/MnO_x nanosheets (Fig. 10a), and the characteristic peaks and the corresponding compounds are listed in Table S3. Part I in Fig. 10a displayed pure toluene adsorption on M-Cu/MnO_x under dark condition. As seen, the characteristic peaks of toluene at light-blue marked region were observed in M-Cu/MnO_x nanosheets. Their intensities rapidly increased with catalyst exposed time till 15 min, demonstrating a high toluene capture ability of M-Cu/MnO_x nanosheets. Part II and part III in Fig. 10a displayed the thermocatalytic and photothermal catalytic processes of toluene degradation under pure thermal-driven and photothermal-driven conditions, respectively. As seen, toluene peaks showed rapid decrease with the rise of a series of new peaks of the oxidation products. For pure thermal-driven condition, toluene was oxidized to benzyl alcohol, benzoic acid and CO₂ (Fig. 10b). Notably, benzyl alcohol (light-green marked region) appeared rapidly at the initial heating time, and then gradually decreased. Meanwhile, the intensity of peaks ascribed to benzoic acid (light-orange marked region) gradually increased within 30 min, while the stretching vibration peaks associated to CO₂ (light-purple marked region) showed almost no increase (part II of Fig. 10a). It showed the occurrence of massive enrichment of benzoic acid molecules, which represented poor catalytic activity of M-Cu/MnO_x for benzoic acid conversion to CO₂ under pure thermal-driven catalytic condition. In comparison, the intensity of CO₂ peaks significantly enhanced from 25 to 30 min under photo-thermal catalytic condition (part III of Fig. 10a), whereas the peaks referred to benzoic acid became

extremely weaker till complete disappearance. These results indicated that thermally catalyzed toluene molecules showed difficulty in ring-opening decomposition and aggregate heavily after conversion to benzoic acid, while photothermal catalysis achieved ring-opening decomposition of toluene molecules. By calculating the mineralization rate based on toluene degradation rate and CO₂ yield (Table S5), it was found that the mineralization rate of photothermal catalysis had been significantly improved compared with thermal catalysis. It indicated that the synergy of photo- and thermo-driven catalysis could generate much greater number of active-OH/-O²⁻ radicals, high-energy hot electrons and abundant active oxygen species [O]. Thus, the degradation performance of toluene in depth was greatly improved.

Moreover, local amplification of in-situ DRIFT spectra for more toluene degraded products is displayed in Fig. S17. Characteristic peaks of benzyl alcohol, benzaldehyde, benzoic acid and maleic anhydride were obviously detected in photothermal catalytic process, and their intensities were not clearly increased. Moreover, these peaks were also detected under pure thermocatalytic condition except for benzoic acid. This verified that the ring opening of benzoic acid was hard to occur, and it might be the rate-determining step in the thermocatalysis [73]. Differently, synergistic effect of photo- and thermo- catalysis could obviously accelerate this step for achieving the deep oxidation of toluene. Thus, almost no aromatic oxidation products accumulated during photothermal catalysis. Based on these findings, the possible reaction paths of toluene in thermocatalysis (path A) and photothermal catalysis (path B) are shown in Fig. 10b. Toluene was difficult to be completely mineralized to benzoic acid in path A. While for photothermal catalytic process, the synergistic effect from photo- and thermo-activation could overcome the energy barrier of ring opening in benzoic acid, and thus was further deeply oxidized to maleic anhydride, CO₂ and H₂O in path B.

4. Conclusions

In summary, polycrystal Cu doped Mn-based oxide nanosheets with abundant interfacial oxygen vacancies were successfully prepared via methanol-induced dimensionality reduction for efficient photothermal catalytic degradation of toluene under high RH. Characterization results revealed that methanol induced flaky crystallinity of manganese oxalate and constructed nanosheeted MnO_x with abundant interfacial oxygen vacancies, Mn³⁺|Mn⁴⁺ oxide polycrystalline and defective meso-micropores structures (416.2 m²·g⁻¹). Meanwhile, in-situ Cu doping effectively promoted the production of more unsaturated metal-O bonds and abundant oxygen vacancies in M-Cu/MnO_x nanosheets. The interfacial oxygen vacancies intensified the internal electron transmission ability, and generated more reactive oxygen species by accelerating the separation of e⁻/h⁺ pairs. Mn³⁺|Mn⁴⁺ oxide polycrystalline was proved to match Z-scheme heterojunction, which could boost redox activity and stability of Mn species and promote more reactive oxygen species by accelerating the separation of e⁻/h⁺ pairs. Synergetic effects of photothermal catalysis investigated by H₂-TPR, O₂-TPD and CO-consumption profiles revealed that M-Cu/MnO_x nanosheets presented higher activation of reduction capability and surface oxygen species. Due to these unique aspects, M-Cu/MnO_x nanosheets exhibited photothermal catalytic toluene conversion of 92.8% and mineralization ratio of 84.4% under vis-light irradiation. The resulting toluene degradation rate reached 3.5–71.9 times higher than many state-of-the-art catalysts. Moreover, M-Cu/MnO_x nanosheets exhibited excellent photothermal catalytic stability toward toluene degradation, showing toluene conversion of 91% and mineralization ratio of 84% respectively after 200 h. Hence, methanol-induced dimensionality and Cu dopant significantly promoted photothermal catalysis of MnO_x toward toluene under high RH and hence can be deemed of high potential for practical applications of VOCs removal.

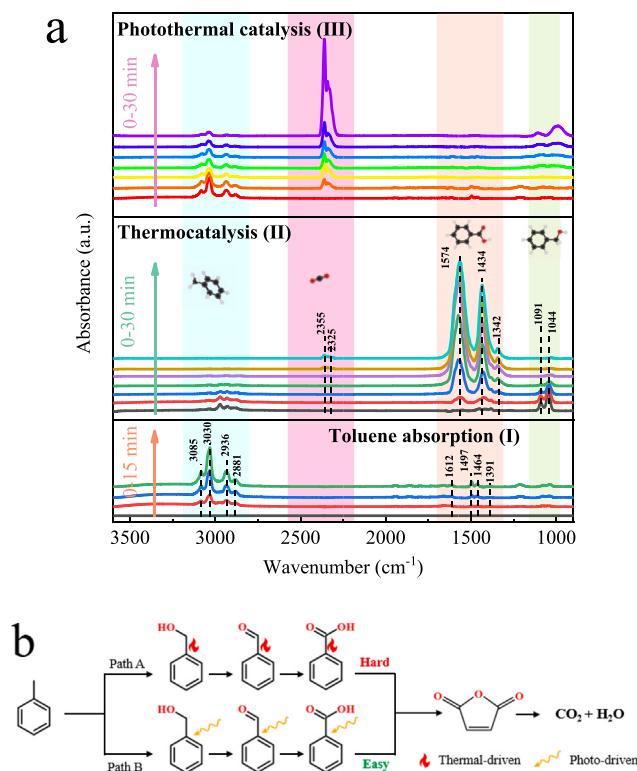


Fig. 10. (a) In-situ DRIFT spectra of M-Cu/MnO_x nanosheets under toluene absorption, thermocatalysis and photothermal catalysis; (b) proposed degradation pathway of toluene.
Proposed reaction pathway.

CRediT authorship contribution statement

S. Jiang conceived the project, devised experiments, conducted experiments, collected the data and processed it, and wrote the manuscript; **C. Li** prepared the materials, conducted experiments, collected the data and analyzed, participated in the discussion and helped to revise the manuscript; **Y. Mohammad** revised the manuscript; **Y. Tang, R. Wang** and **J. Li** analyzed data and helped to revise the manuscript; **J. Li** provide much advice on the project, **Z. Zhao** and **Z. Zhao** conceived the project, discussion and revised the manuscript.

Declaration of Competing Interest

The authors declare that they have no known competing financial interests or personal relationships that could have appeared to influence the work reported in this paper.

Data Availability

No data was used for the research described in the article.

Acknowledgments

This work was financially supported by the National Natural Science Foundation of China (No. 22178073, 21968003, 22268004, and 22172039), and the Natural Science Foundation of Guangxi Province (No. 2020GXNSFGA297001 and 2022GXNSFAA035464). State Key Laboratory of Featured Metal Materials and Life-cycle Safety for Composite Structures. Special Funding for “Bagui Scholars Program of Guangxi Zhuang Autonomous Region” Guangxi Distinguished Experts Special Foundation of China (No. 2019A33).

Appendix A. Supporting information

Supplementary data associated with this article can be found in the online version at [doi:10.1016/j.apcatb.2023.122509](https://doi.org/10.1016/j.apcatb.2023.122509).

References

- [1] C. He, J. Cheng, X. Zhang, M. Douthwaite, S. Pattisson, Z. Hao, Recent advances in the catalytic oxidation of volatile organic compounds: a review based on pollutant sorts and sources, *Chem. Rev.* 119 (2019) 4471–4568.
- [2] M.S. Kamal, S.A. Razzak, M.M. Hossain, Catalytic oxidation of volatile organic compounds (VOCs) - a review, *Atmos. Environ.* 140 (2016) 117–134.
- [3] J. Wang, Y. Muhammad, Z. Gao, S.J. Shah, S. Nie, L. Kuang, Z. Zhao, Z. Qiao, Z. Zhao, Implanting polyethylene glycol into MIL-101(Cr) as hydrophobic barrier for enhancing toluene adsorption under highly humid environment, *Chem. Eng. J.* 404 (2021), 126562.
- [4] Z. Gao, J. Wang, Y. Muhammad, Y. Zhang, S.J. Shah, Y. Hu, Z. Chu, Z. Zhao, Z. Zhao, Enhanced moisture-resistance and excellent photocatalytic performance of synchronous N/Zn-decorated MIL-125(Ti) for vaporous acetaldehyde degradation, *Chem. Eng. J.* 388 (2020), 124389.
- [5] P. Hu, R. Wang, Z. Gao, S. Jiang, Z. Zhao, H. Ji, Z. Zhao, Improved interface compatibility of hollow H-Zr_{0.1}Ti_{0.9}O₂ with UiO-66-NH₂ via Zr-Ti bidirectional penetration to boost visible photocatalytic activity for acetaldehyde degradation under high humidity, *Appl. Catal. B-Environ.* 296 (2021), 120371.
- [6] W.-C. Cho, K.-M. Poo, H.O. Mohamed, T.-N. Kim, Y.-S. Kim, M.H. Hwang, D.-W. Jung, K.-J. Chae, Non-selective rapid electro-oxidation of persistent, refractory VOCs in industrial wastewater using a highly catalytic and dimensionally stable Ir/Pd/Ti composite electrode, *Chemosphere* 206 (2018) 483–490.
- [7] L. Wei, C. Yu, K. Yang, Q. Fan, H. Ji, Recent advances in VOCs and CO removal via photothermal synergistic catalysis, *Chinese. J. Catal.* 42 (2021) 1078–1095.
- [8] R. Ma, J. Sun, D.H. Li, J.J. Wei, Review of synergistic photo-thermo-catalysis: mechanisms, materials and applications, *Int. J. Hydrol. Energy* 45 (2020) 30288–30324.
- [9] P. Wu, X. Jin, Y. Qiu, D. Ye, Recent progress of thermocatalytic and photo/thermocatalytic oxidation for VOCs purification over manganese-based oxide catalysts, *Environ. Sci. Technol.* 55 (2021) 4268–4286.
- [10] L. Imranul I, H. Zaher, P. John H, A. James E, N. Mark, Modeling the effect of relative humidity on adsorption dynamics of volatile organic compound onto activated carbon, *Environ. Sci. Technol.* 53 (2019) 2647–2659.
- [11] T.-Y. Li, S.-J. Chiang, B.-J. Liaw, Y.-Z. Chen, Catalytic oxidation of benzene over CuO/Ce_{1-x}Mn_xO₂ catalysts, *Appl. Catal. B-Environ.* 103 (2011) 143–148.
- [12] W. Yang, Za Su, Z. Xu, W. Yang, Y. Peng, J. Li, Comparative study of α , β , γ and δ -MnO₂ on toluene oxidation: Oxygen vacancies and reaction intermediates, *Appl. Catal. B-Environ.* 260 (2020), 118150.
- [13] E. Yu, J. Chen, H. Jia, Enhanced light-driven photothermocatalytic activity on selectively dissolved LaTi_{1-x}Mn_xO₃₊₈ perovskites by photoactivation, *J. Hazard. Mater.* 399 (2020), 122942.
- [14] X. Zhang, F. Bi, Z. Zhu, Y. Yang, S. Zhao, J. Chen, X. Lv, Y. Wang, J. Xu, N. Liu, The promoting effect of H₂O on rod-like MnCeO_x derived from MOFs for toluene oxidation: a combined experimental and theoretical investigation, *Appl. Catal. B-Environ.* 297 (2021), 120393.
- [15] P. Wu, S. Dai, G. Chen, S. Zhao, Z. Xu, M. Fu, P. Chen, Q. Chen, X. Jin, Y. Qiu, S. Yang, D. Ye, Interfacial effects in hierarchically porous alpha-MnO₂/Mn₃O₄ heterostructures promote photocatalytic oxidation activity, *Appl. Catal. B-Environ.* 268 (2020), 118418.
- [16] J.-J. Li, E.-Q. Yu, S.-C. Cai, X. Chen, J. Chen, H.-P. Jia, Y.-J. Xu, Noble metal free, CeO₂/LaMnO₃ hybrid achieving efficient photo-thermal catalytic decomposition of volatile organic compounds under IR light, *Appl. Catal. B-Environ.* 240 (2019) 141–152.
- [17] A. Verma, R. Kore, D.R. Corbin, M.B. Shiflett, Metal recovery using oxalate chemistry: a technical review, *Ind. Eng. Chem. Res* 58 (2019) 15381–15393.
- [18] W. Tang, X. Wu, D. Li, Z. Wang, G. Liu, H. Liu, Y. Chen, Oxalate route for promoting activity of manganese oxide catalysts in total VOCs' oxidation: effect of calcination temperature and preparation method, *J. Mater. Chem. A* 2 (2014) 2544–2554.
- [19] X. Ma, J. Li, M.A. Rankin, L.M. Croll, J.R. Dahn, Highly porous MnO_x prepared from Mn(C₂O₄)·3H₂O as an adsorbent for the removal of SO₂ and NH₃, *Microporous Mesoporous Mater.* 244 (2017) 192–198.
- [20] Z.-G. Jia, L.-H. Yue, Y.-F. Zheng, Z.-D. Xu, Crystallization behavior and thermal decomposition characteristics of manganese(II) oxalate in organic-water binary solvent system, *Chin. J. Inorg. Chem.* 23 (2007) 181–188.
- [21] M. Zhang, K. Xu, X.S. Jiang, L. Yang, G. He, X.P. Song, Z.Q. Sun, J.G. Lv, Effect of methanol ratio in mixed solvents on optical properties and wettability of ZnO films by cathodic electrodeposition, *J. Alloy. Compd.* 615 (2014) 327–332.
- [22] R.T. Dong, H.L. Wang, Q. Zhang, X.T. Xu, F. Wang, B. Li, Shape-controlled synthesis of Mn₂O₃ hollow structures and their catalytic properties, *Crystengcomm* 17 (2015) 7406–7413.
- [23] M.R. Morales, B.P. Barbero, L.E. Cadus, Total oxidation of ethanol and propane over Mn-Cu mixed oxide catalysts, *Appl. Catal. B-Environ.* 67 (2006) 229–236.
- [24] X. Chen, Q. Li, M. Zhang, J.J. Li, S.C. Cai, J. Chen, H.P. Jia, MOF-templated preparation of highly dispersed Co/Al₂O₃ composite as the photothermal catalyst with high solar-to-fuel efficiency for CO₂ methanation, *ACS Appl. Mater. Interfaces* 12 (2020) 39304–39317.
- [25] W.Z. Wang, C.K. Xu, G.H. Wang, Y.K. Liu, C.L. Zheng, Preparation of smooth single-crystal Mn₃O₄ nanowires, *Adv. Mater.* 14 (2002) 837–840.
- [26] R. Cao, L. Li, P. Zhang, L. Gao, S. Rong, Regulating oxygen vacancies in ultrathin delta-MnO₂ nanosheets with superior activity for gaseous ozone decomposition, *Environ. Sci. Nano* 8 (2021) 1628–1641.
- [27] H. Zhao, X.X. Zhou, L.Y. Pan, M. Wang, H.R. Chen, J.L. Shi, Facile synthesis of spinel Cu_{1.5}Mn_{1.5}O₄ microspheres with high activity for the catalytic combustion of diesel soot, *RSC Adv.* 7 (2017) 20451–20459.
- [28] T. Chang, Z.X. Shen, Y. Huang, J.Q. Lu, D.X. Ren, J. Sun, J.J. Cao, H.X. Liu, Post-plasma-catalytic removal of toluene using MnO₂-Co₃O₄ catalysts and their synergistic mechanism, *Chem. Eng. J.* 348 (2018) 15–25.
- [29] Y.-N. Chan, H.-K. Zhao, X.-G. Wang, X.-J. Zhao, catena-Poly bis(N,N-dimethylformamide)-manganese(II) -di- μ_2 -oxalato, *Acta Cryst.* 63 (2007) M70–M72.
- [30] Y.N. Zhang, S.S. Li, H.X. Kuai, Y.F. Long, X.Y. Lv, J. Su, Y.X. Wen, Proton solvent-controllable synthesis of manganese oxalate anode material for lithium-ion batteries, *RSC Adv.* 11 (2021) 23259–23269.
- [31] G. Li, Z. Huang, J. Chen, F. Yao, J. Liu, O.L. Li, S. Sun, Z. Shi, Rechargeable Zn-ion batteries with high power and energy densities: a two-electron reaction pathway in birnessite MnO₂ cathode materials, *J. Mater. Chem. A* 8 (2020) 1975–1985.
- [32] D. Yan, S. Cheng, R.F. Zhuo, J.T. Chen, J.J. Feng, H.T. Feng, H.J. Li, Z.G. Wu, J. Wang, P.X. Yan, Nanoparticles and 3D sponge-like porous networks of manganese oxides and their microwave absorption properties, *Nanotechnology* 20 (2009), 105706.
- [33] J.C. Jia, X. Lian, M.Z. Wu, F.C. Zheng, Y.H. Gao, H.L. Niu, Self-assembly of alpha-MnO₂/Mn₃O₄ hierarchical structure on carbon cloth for asymmetric supercapacitors, *J. Mater. Sci.* 56 (2021) 3246–3255.
- [34] Y. Xu, Z. Qu, Y. Ren, C. Dong, Enhancement of toluene oxidation performance over Cu-Mn composite oxides by regulating oxygen vacancy, *Appl. Surf. Sci.* 560 (2021), 149883.
- [35] L. Yang, S. Cheng, J. Wang, X. Ji, Y. Jiang, M. Yao, P. Wu, M. Wang, J. Zhou, M. Liu, Investigation into the origin of high stability of delta-MnO₂ pseudo-capacitive electrode using operando Raman spectroscopy, *Nano Energy* 30 (2016) 293–302.
- [36] Z.M. Chan, D.A. Kitchaev, J.N. Weker, C. Schnedermann, K. Lim, G. Ceder, W. Tumas, M.F. Toney, D.G. Nocera, Electrochemical trapping of metastable Mn³⁺ ions for activation of MnO₂ oxygen evolution catalysts, *Proc. Natl. Acad. Sci. USA* 115 (2018) E5261–E5268.
- [37] X.R. Liang, J.E. Post, B. Lanson, X.M. Wang, M.Q. Zhu, F. Liu, W.F. Tan, X.H. Feng, G.M. Zhu, X. Zhang, J.J. De Yoreo, Coupled morphological and structural evolution of delta-MnO₂ to alpha-MnO₂ through multistage oriented assembly processes: the role of Mn(iii), *Environ. Sci. -Nano* 7 (2020) 238–249.

[38] W. Gu, C. Li, J. Qiu, J. Yao, Facile fabrication of flower-like MnO_2 hollow microspheres as high-performance catalysts for toluene oxidation, *J. Hazard. Mater.* 408 (2021), 124458.

[39] C. Lee, B.G. Jeong, S.J. Yun, Y.H. Lee, S.M. Lee, M.S. Jeong, Unveiling defect-related raman mode of monolayer WS_2 via tip-enhanced resonance Raman Scattering, *ACS Nano* 12 (2018) 9982–9990.

[40] A.P. Meilakhs, S.V. Koniakhin, New explanation of Raman peak redshift in nanoparticles, *Superlattices Micro* 110 (2017) 319–323.

[41] Z. Zhong, M. Li, J. Fu, Y. Wang, Y. Muhammad, S. Li, J. Wang, Z. Zhao, Construction of Cu-bridged $\text{Cu}_2\text{O}/\text{MIL}(\text{Fe}/\text{Cu})$ catalyst with enhanced interfacial contact for the synergistic photo-Fenton degradation of thiacloprid, *Chem. Eng. J.* 395 (2020), 125184.

[42] B. Donkova, J. Pencheva, M. Djarova, Influence of complex formation upon inclusion of Mn(II), Co(II), Ni(II), and Cu(II) in $\text{ZnC}_2\text{O}_4\text{-H}_2\text{O}$, *Cryst. Res. Technol.* 39 (2004) 207–213.

[43] S. Mo, Q. Zhang, J. Li, Y. Sun, Q. Ren, S. Zou, Q. Zhang, J. Lu, M. Fu, D. Mo, J. Wu, H. Huang, D. Ye, Highly efficient mesoporous MnO_2 catalysts for the total toluene oxidation: oxygen-Vacancy defect engineering and involved intermediates using in situ DRIFTS, *Appl. Catal. B-Environ.* 264 (2020), 118464.

[44] J. Hou, Y. Li, L. Liu, L. Ren, X. Zhao, Effect of giant oxygen vacancy defects on the catalytic oxidation of OMS-2 nanorods, *J. Mater. Chem. A* 1 (2013) 6736–6741.

[45] L. Kang, C. Huang, J. Zhang, M.Y. Zhang, N. Zhang, Y.Q. He, C. Luo, C.L. Wang, X. F. Zhou, X. Wu, A new strategy for synthesis of hierarchical $\text{MnO}_2\text{-Mn}_3\text{O}_4$ nanocomposite via reduction-induced exfoliation of MnO_2 nanowires and its application in high-performance asymmetric supercapacitor, *Compos. Part B Eng.* 178 (2019), 107501.

[46] E. Yu, J. Li, J. Chen, J. Chen, Z. Hong, H. Jia, Enhanced photothermal catalytic degradation of toluene by loading Pt nanoparticles on manganese oxide: photoactivation of lattice oxygen, *J. Hazard. Mater.* 388 (2020), 121800.

[47] M. Zhang, H. Gao, J. Chen, E.A. Elimian, H. Jia, Calcination engineering of urchin-like $\text{CoO}_x\text{-CN}$ catalysts to enhance photothermocatalytic oxidation of toluene via photo-/thermo- coupling effect, *Appl. Catal. B-Environ.* 307 (2022), 121208.

[48] C. Jiang, H. Wang, Y. Wang, C. Xue, Z. Yang, C. Yu, H. Ji, Modifying defect States in CeO_2 by Fe doping: A strategy for low-temperature catalytic oxidation of toluene with sunlight, *J. Hazard. Mater.* 390 (2020), 122182.

[49] D.-S. Liu, Y. Mai, S. Chen, S. Liu, E.H. Ang, M. Ye, Y. Yang, Y. Zhang, H. Geng, C. Li, A ^{1}D - ^{3}D interconnected $\delta\text{-MnO}_2$ nanowires network as high-performance and high energy efficiency cathode material for aqueous zinc-ion batteries, *Electrochim. Acta* 370 (2021), 137740.

[50] J.J. Li, S.C. Cai, E.Q. Yu, B. Weng, X. Chen, J. Chen, H.P. Jia, Y.J. Xu, Efficient infrared light promoted degradation of volatile organic compounds over photo-thermal responsive Pt-rGO-TiO₂ composites, *Appl. Catal. B Environ.* 233 (2018) 260–271.

[51] X.A. Dong, W. Cui, H. Wang, J.Y. Li, Y.J. Sun, H.N. Wang, Y.X. Zhang, H.W. Huang, F. Dong, Promoting ring-opening efficiency for suppressing toxic intermediates during photocatalytic toluene degradation via surface oxygen vacancies, *Sci. Bull.* 64 (2019) 669–678.

[52] W.J. Xu, X. Chen, J. Chen, H.P. Jia, Bimetal oxide $\text{CuO}/\text{Co}_3\text{O}_4$ derived from Cu ions partly-substituted framework of ZIF-67 for toluene catalytic oxidation, *J. Hazard. Mater.* 403 (2021), 123869.

[53] J. Li, M. Zhang, E.A. Elimian, X. Lv, J. Chen, H. Jia, Convergent ambient sunlight-powered multifunctional catalysis for toluene abatement over in situ exsolution of Mn_3O_4 on perovskite parent, *Chem. Eng. J.* 412 (2021), 128560.

[54] E.A. Elimian, M. Zhang, J. Chen, H. Jia, Y. Sun, J. He, Construction of Pt-mTiO₂/USY multifunctional catalyst enriched with oxygen vacancies for the enhanced light-driven photothermocatalytic degradation of toluene, *Appl. Catal. B Environ.* 307 (2022), 121203.

[55] H. Yu, J. Li, Y. Zhang, S. Yang, K. Han, F. Dong, T. Ma, H. Huang, Three-in-one oxygen vacancies: whole visible-spectrum absorption, efficient charge separation, and surface site activation for robust CO_2 photoreduction, *Angew. Chem. Int. Ed.* 58 (2019) 3880–3884.

[56] M. Kim, B. Lee, H. Ju, J.Y. Kim, J. Kim, S.W. Leek, Oxygen-vacancy-introduced $\text{BaSnO}_{3.8}$ photoanodes with tunable band structures for efficient solar-driven water splitting, *Adv. Mater.* 31 (2019) 1903316.

[57] A. Burcu, D. Gokhan, E. Metehan, K. Ishak, Formation and characterization of infrared absorbing copper oxide surfaces, *Appl. Surf. Sci.* 30 (2017) 218–224.

[58] J. Li, M. Zhang, Z. Guan, Q. Li, C. He, J. Yang, Synergistic effect of surface and bulk single-electron-trapped oxygen vacancy of TiO_2 in the photocatalytic reduction of CO_2 , *Appl. Catal. B-Environ.* 206 (2017) 300–307.

[59] P.L. Popa, J. Crepelriere, P. Nukala, R. Leturcq, D. Lenoble, Invisible electronics: metastable Cu-vacancies chain defects for highly conductive p-type transparent oxide, *Appl. Mater. Today* 9 (2017) 184–191.

[60] W. Zhang, Y. Chen, G. Zhang, X. Tan, Q. Ji, Z. Wang, H. Liu, J. Qu, Hot-electron-induced photothermal catalysis for energy-dependent molecular oxygen activation, *Angew. Chem. Int. Ed.* 60 (2021) 4872–4878.

[61] Z.Q. Wang, H.Z. Jia, T. Zheng, Y.C. Dai, C. Zhang, X.T. Guo, T.C. Wang, L.Y. Zhu, Promoted catalytic transformation of polycyclic aromatic hydrocarbons by MnO_2 polymorphs: Synergistic effects of Mn^{3+} and oxygen vacancies, *Appl. Catal. B-Environ.* 272 (2020), 119030.

[62] Y. Wang, Z. Zhong, Y. Muhammad, H. He, Z. Zhao, S. Nie, Z. Zhao, Defect engineering of $\text{NH}_2\text{-MIL}-88\text{B}(\text{Fe})$ using different monodentate ligands for enhancement of photo-Fenton catalytic performance of acetamiprid degradation, *Chem. Eng. J.* 398 (2020), 125684.

[63] J. Zhao, Z. Zhao, N. Li, J. Nan, R. Yu, J. Du, Visible-light-driven photocatalytic degradation of ciprofloxacin by a ternary $\text{Mn}_2\text{O}_3/\text{Mn}_3\text{O}_4/\text{MnO}_2$ valence state heterojunction, *Chem. Eng. J.* 353 (2018) 805–813.

[64] Z. Zhang, Y. Muhammad, Y. Chen, S.J. Shah, Y. Peng, S. Shao, R. Wang, X. Li, H. Liu, Z. Zhao, Construction of ultra-stable and Z-scheme Fe-Graphdiyne/MIL-100 (Fe) photo-Fenton catalyst with C = C-Fe|O interface for the highly enhanced catalytic degradation of Dinoflagellate, *Chem. Eng. J.* 426 (2021), 131621.

[65] Q. Xu, L. Zhang, B. Cheng, J. Fan, J. Yu, S-scheme heterojunction photocatalyst, *Chem* 6 (2020) 1543–1559.

[66] J.X. Low, J.G. Yu, M. Jaroniec, S. Wageh, A.A. Al-Ghamdi, Heterojunction photocatalysts, *Adv. Mater.* 29 (2017) 1601694.

[67] X. Hu, Y. Ye, W. Dong, Y. Huang, M. Zhu, Quantitative evaluation of structure-activity relationships in heterogeneous photocatalytic oxidation towards organic contaminants, *Appl. Catal. B-Environ.* 309 (2022), 121238.

[68] J.L. Wang, J.E. Li, C.J. Jiang, P. Zhou, P.Y. Zhang, J.G. Yu, The effect of manganese vacancy in birnessite-type MnO_2 on room-temperature oxidation of formaldehyde in air, *Appl. Catal. B Environ.* 204 (2017) 147–155.

[69] L. Yang, Q. Liu, R. Han, K. Fu, Y. Su, Y. Zheng, X. Wu, C. Song, N. Ji, X. Lu, D. Ma, Confinement and synergy effect of bimetallic Pt-Mn nanoparticles encapsulated in ZSM-5 zeolite with superior performance for acetone catalytic oxidation, *Appl. Catal. B-Environ.* 309 (2022), 121224.

[70] S.L. Yang, H.C. Yang, J.Y. Yang, H.L. Qi, J. Kong, Z. Bo, X.D. Li, J.H. Yan, K.F. Cen, X. Tu, Three-dimensional hollow urchin alpha- MnO_2 for enhanced catalytic activity towards toluene decomposition in post-plasma catalysis, *Chem. Eng. J.* 402 (2020), 126154.

[71] S. Kazutaka, T. Makoto, Y. Kimihisa, Enhanced catalytic performance of subnano copper oxide particles, *ACS Nano* 14 (2020) 1804–1810.

[72] Y. Wang, N. Xu, D. Li, J. Zhu, Thermal properties of two dimensional layered materials, *Adv. Funct. Mater.* 27 (2017) 1604134.

[73] F. Wang, J. Deng, S. Impeng, Y.J. Shen, T.T. Yan, G.R. Chen, L.Y. Shi, D.S. Zhang, Unraveling the effects of the coordination number of Mn over alpha- MnO_2 catalysts for toluene oxidation, *Chem. Eng. J.* 396 (2020), 125192.